J. Fluid Mech. (2003), *vol.* 490, *pp.* 37–74.
DOI: 10.1017/S0022112003005251 Printed in the United Kingdom

Spanwise structure and scale growth in turbulent boundary layers

By C. D. TOMKINS† AND R. J. ADRIAN

Department of Theoretical and Applied Mechanics, University of Illinois at Urbana-Champaign, Urbana, IL 61801, USA

(Received 13 August 2002 and in revised form 18 April 2003)

Spanwise structure and growth mechanisms in a turbulent boundary layer are investigated experimentally. PIV measurements are obtained in the streamwise–spanwise (x–z)-plane from the buffer layer to the top of the logarithmic region at $Re_\theta = 1015$ and 7705. The dominant motions of the flow are shown to be large-scale regions of momentum deficit elongated in the streamwise direction. Throughout the logarithmic layer, the regions are consistently bordered by vortices organized in the streamwise direction, offering strong support for a vortex packet model. Additionally, evidence is presented for the existence and organization of hairpin vortices in the region $y^+ < 60$. Statistical evidence is also presented for two important aspects of the vortex packet paradigm: vortex organization in the streamwise direction, and the clear association of the hairpin signature with local minima in streamwise velocity. Several spanwise lengthscales are shown to vary linearly with distance from the wall, revealing self-similar growth of spanwise structure in an average sense. Inspection of the data, however, suggests that individual structures do not grow strictly self-similarly in time. It is proposed that additional scale growth occurs by the merging of vortex packets on an eddy-by-eddy basis via a vortex re-connection mechanism similar to that suggested by Wark & Nagib (1989). The proposed mechanism provides a link between vortex-pairing concepts and the observed coalescence of streaky low-speed regions in the inner layer.

1. Introduction

The seemingly random perturbations and fluctuations present in the flow of fluid over a wall contain a significant element of order or coherence. Near-wall measurements reveal a high degree of order for $y^+ = y/y^* < 30$ (e.g. Kline *et al.* 1967; Smith & Metzler 1983), and recent measurements reveal a surprising degree of vortex organization in the logarithmic region as well (Adrian, Meinhart & Tomkins 2000*b*, hereafter referred to as AMT). (Here $y^* = \nu/u_\tau$ represents the viscous lengthscale, where ν is the kinematic viscosity and $u_\tau = \sqrt{\tau_w/\rho}$ is the wall friction velocity; τ_w denotes the wall shear stress and ρ the density.) A fully three-dimensional understanding of these flow structures, however, remains elusive, and several important issues remain unresolved. One set of issues addresses the nature and growth of structures in the spanwise direction. Understanding behaviour in this third

† Present address: Los Alamos National Laboratory, DX-3, MS P940, Los Alamos, NM 87545, USA.

(spanwise) dimension is a crucial ingredient in obtaining a thorough understanding of the boundary layer.

1.1. *Spanwise character of inner-layer structure*

Low-speed streaks are the most important spanwise structure in the near-wall region. The spacing of these streaks, and how it varies with Reynolds number and distance from the wall, are important issues in understanding scale growth. Kline *et al.* (1967) visualized the streaks and showed that near the wall the mean streak spacing is $\overline{\lambda_z^+} \approx 100$, a figure that has since been verified many times at low Reynolds number (the superscript $^+$ denotes normalization by inner units). In visual studies, Smith & Metzler (1983) reported $\overline{\lambda_z^+} \approx 100$ up to $Re_\theta = U_\infty \theta/\nu \approx 5800$, where U_∞ denotes the free-stream velocity and θ the momentum thickness, and showed that the mean spacing increases with distance from the wall up to $y^+ = 30$. This increase has been verified and shown to be linear in the channel flow simulations of Kim, Moin & Moser (1987). More recently, Klewicki *et al.* (1995) performed visualizations in the atmospheric boundary layer that confirmed $\overline{\lambda_z^+} \approx 100$ up to $Re_\theta \approx 1.5 \times 10^6$. There is also consensus in the literature on the existence of quasi-streamwise vortices in close proximity to the low-speed regions. These vortices are observed to have long streamwise extent, and they pump low-speed fluid from the wall, with a wall-normal core location in the range $y^+ \approx 20$–40 (Blackwelder & Eckelmann 1979; Smith & Schwartz 1983; Kasagi, Hirata & Nishino 1986; Kasagi 1988).

A structure that is closely related to the quasi-streamwise vortices is the hairpin-type vortex. First proposed as a horseshoe vortex that developed from stretching of perturbed spanwise vorticity (Theodorsen 1952), the hairpin model has gained widespread, although not universal, acceptance over the past few decades. In its modern version, the observed quasi-streamwise vortices are the legs of hairpins, which are typically idealized as symmetric but in reality may be one-sided (or 'cane-like') or two-sided but asymmetric. The low-speed streaks are generated by the induction of the vortex legs, pumping low-speed fluid upwards, as observed in Blackwelder & Eckelmann (1979). For a summary of evidence for the existence of hairpins, the reader is referred to the report of Wallace (1982), an update three years later (Wallace 1985), and the review of Robinson (1991).

Perhaps the most convincing evidence in favour of hairpins in the near-wall region at low Reynolds number is the systematic set of visual experiments performed by Smith and co-workers over a period of several years, and synthesized into a model by Smith (1984). The hydrogen-bubble visualizations of Smith & Metzler (1983) were an important aspect of this model; they revealed vortex loops in association with the streaks in the region $5 < y^+ < 35$. Furthermore, the streaks were occasionally observed to oscillate and break down, forming a series of 2–5 hairpin-like structures near the wall.

Evidence has also accumulated for the existence of hairpin vortices in the outer region. Head & Bandyopadhyay (1981) performed seminal flow visualization measurements with an inclined light sheet, showing that loop vortices densely populate the outer region of the boundary layer at elevated Reynolds number. More recently, AMT obtained particle image velocimetry (PIV) measurements in the streamwise–wall-normal (x–y)-plane of a turbulent boundary layer at low and high Reynolds number. Among other things, the data provided quantitative evidence for the existence of hairpin-type vortices in the logarithmic region and above.

The existence of hairpins in the buffer region, however, is not universally accepted. For example, Heist, Hanratty & Na (2000) examined direct numerical simulation

(DNS) results of a turbulent channel flow, focusing on the region $y^+ < 60$. They concluded that the dominant structures are individual quasi-streamwise vortices, and observed a mechanism for the creation of these vortices by the turning of arch vortices. In their view, a hairpin interpretation is not necessary to explain near-wall observations. It will be seen, however, that the present observations cannot be explained solely by quasi-streamwise vortices.

1.2. *Spanwise character of large-scale structure*

Coherent large-scale motions have been observed over a range of Reynolds numbers. At low Reynolds number, the well-known turbulent 'bulges' of fluid are observed in the outer region (Kovasznay, Kibens & Blackwelder 1970; Nychas, Hershey & Brodkey 1973). The bulges define the corrugated edge of the boundary layer and are highly three-dimensional.

Observations of large-scale structure at higher Reynolds number are also reported. Wark & Nagib (1991) investigated a $Re_\theta = 4650$ boundary layer using conditional averaging of all velocity components in three dimensions. They observed 'roller-type' structures extending several δ streamwise and approximately 0.5δ spanwise (where δ is the boundary-layer thickness). These motions had been observed previously and associated with Reynolds stress production (Guezennec 1985). Meinhart & Adrian (1995) performed high-resolution PIV measurements in the $(x{-}y)$-plane of a boundary layer over a range of Reynolds numbers up to $Re_\theta = 6845$. The instantaneous measurements revealed large regions or 'zones' in which the streamwise momentum was roughly uniform. Regions of elevated $\partial U/\partial y$ appeared between adjacent zones. Tomkins (1997) performed additional measurements over a similar range of Reynolds numbers, but with a wider streamwise field of view, approximately 3δ. At $Re_\theta \approx 7700$, the zones were observed to angle upwards from the wall at roughly 10–20°, forming a ramp-like shape. Larger, presumably older, ramps typically extended approximately δ–1.5δ streamwise and out to $y/\delta \approx 0.4$–0.6. Hairpin-type vortices were observed on the upstream edge of these motions. A three-dimensional understanding of these large-scale motions and their characteristics, however, remains elusive, and is one of the goals of the present work.

Several authors have evaluated the importance of the large scales in terms of the turbulent kinetic energy. Naguib & Wark (1992) performed hot-wire measurements over a range of Reynolds numbers up to $Re_\theta \approx 6000$. The data reveal that the large scales dominate the energy, although wall eddies contribute more to the Reynolds stress. Tomkins & Adrian (2003) examined the streamwise and spanwise energy distribution in the near-wall region of a low-Reynolds-number turbulent boundary layer. Measurements reveal that while the established $\lambda_z^+ = 100$ mode is energetic, much larger spanwise modes actually contribute more to the streamwise turbulent kinetic energy, even at $y^+ = 21$. Tomkins & Adrian also measured a higher-Reynolds-number layer, comparable to the layer in Naguib & Wark, and demonstrated the energetic dominance of the large spanwise scales throughout the logarithmic region. The large spanwise scales were shown to be related to the large streamwise scales, on average, providing a link to the results of Naguib & Wark.

Despite these gains in understanding, two of the most fundamental, and important, questions remain in unresolved: *What* are the large-scale structures, and *how* are they created? Several models have been proposed. The well-known model of Perry and co-workers (Perry & Chong 1982; Perry, Henbest & Chong 1986; Marusic & Perry 1995) depicts the boundary layer as a forest of lambda-type vortices. This model captures many important aspects of boundary-layer behaviour, but does not account

for the very large streamwise scales. Wark & Nagib (1991) interpreted the large motions in their boundary layer as extended double 'roller-type' structures, similar to those originally proposed by Townsend (1976).

The idea that smaller scales organize to create the larger scales has gathered increasing support over the past two decades. The flow visualization measurements of Head & Bandyopadhyay (1981) revealed groups of inclined vortex structures along the outer edge of the boundary layer, and the model of Smith (1984) provides evidence of this organization near the wall. Repeated quantitative observations of large-scale organization throughout the layer were not reported, however, until the measurements of AMT. The authors report the frequent occurrence of organized hairpin-type vortices in the outer region over a range of Reynolds numbers, as viewed in the $(x–y)$-plane. These 'packets' of vortices are interpreted to work cooperatively to induce large regions of streamwise momentum deficit, thus providing a mechanism for the formation of the uniform momentum zones observed by Meinhart & Adrian (1995). Furthermore, when the envelope of the vortex heads grows linearly from the wall, the associated low-speed region assumes a ramp-like shape, as observed in Tomkins (1997). Marusic (2001) extends the attached-eddy model of Perry & Marusic (1995) to investigate implications of the vortex packet paradigm. The results suggest that streamwise vortex organization is important for Reynolds stresses and transport processes in the logarithmic layer. This organization is not without a physical basis; mechanisms for organization via vortex generation are suggested by Smith *et al.* (1991) and Zhou *et al.* (1999).

1.3. *Mechanisms of spanwise growth*

The evidence put forth in AMT and the vortex packet model address key aspects of the important questions given earlier (e.g. how the large streamwise scales are created). A fully three-dimensional understanding of the large-scale motions and associated growth mechanisms at elevated Reynolds number, however, is not at hand. Experimental observations of scale growth in the spanwise direction are particularly scarce; as a result, the identification of spanwise growth mechanisms has proven very difficult.

Conclusive results on this issue remain buried near the wall. Nakagawa & Nezu (1981) observed streaks merging and splitting in equilibrium at $y^+ \approx 5$. Further from the wall, in the region $y^+ > 30$, having observed increased streak spacing, they conjecture that coalescence of streaks prevails over division to create scale growth. Smith & Metzler (1983) also report extensively on streak coalescence and division. Mergings of streaks are most pronounced in the region $10 < y^+ < 30$, while divisions are particularly frequent near $y^+ = 15$. Occasionally, streaks were observed to merge, only to divide at some later time. The authors note, however, that the structure becomes much more complex with distance from the wall, so that attempts to quantify streak spacing, mergings, or divisions become too subjective. Like Nakagawa & Nezu, Smith & Metzler conjecture merging as a mechanism for scale growth above $y^+ = 30$; however, no direct observation of merging is reported for $y^+ > 30$.

1.4. *The present study: approach and objectives*

The goal of the present study is to understand the mechanisms by which scale growth occurs in the spanwise direction, coupled with scale growth in the vertical direction. A second goal is to build upon available results to obtain an improved three-dimensional understanding of boundary-layer structure.

To this end, wide-view particle image velocimetry (Adrian 1991) measurements are performed in the streamwise–spanwise (x–z)-plane of a turbulent boundary layer at $Re_\theta = 1015$ and 7705. Emphasis is placed on the structure of the $Re_\theta = 7705$ layer; here Reynolds number effects are minimal (by conventional wisdom), and the flow more closely reflects most applications. The $Re_\theta = 1015$ measurements are complementary, providing insight closer to the wall and superior resolution of the smaller scales. Digital PIV measurements are obtained at several heights for each Reynolds number; measurement locations range from the near-wall region ($y^+ = 21$) to the top of the logarithmic layer ($y/\delta = 0.2$). Two digital cameras (2k by 2k) are placed side-by-side in z to capture the largest spanwise scales. Additional measurements are obtained with film-based PIV at a few selected heights. These high-resolution measurements feature a view of several δ in both x and z, allowing simultaneous observation of large-scale motions and the associated small scales.

The measurements are used for quantitative flow visualization and statistical analysis. In the following sections, we identify the dominant large-scale motions of the layer, and report their spanwise and streamwise characteristics as a function of distance from the wall. The data are consistent with the vortex packet model of AMT. The association of the large-scale motions with groups of streamwise-aligned vortices is established, and the vortex packet characteristics are described. Several spanwise lengthscales are calculated, and shown to vary linearly with wall-normal distance. Instantaneous results, however, suggest that individual structures do not strictly grow self-similarly in time. A mechanism for additional spanwise growth involving the merger of vortex packets is then presented. This model is conceptually similar to the Λ-vortex growth model of Perry & Chong (1982) and the spanwise-merger hairpin vortex model proposed in Wark & Nagib (1989). It is also consistent with the recent computational (DNS) results of Adrian, Balachander & Liu (2001), which clearly show the spanwise merger of hairpin-type structures in a channel, and establish that the time for viscous vortex re-connection is small relative to the evolutionary time-scale of the packets. Finally, instantaneous fields of velocity and swirling strength are presented, which contain patterns that are consistent with the proposed growth mechanism throughout the logarithmic region.

2. Experiment

2.1. *Flow facility and parameters*

Measurements are performed in a low-turbulence open-circuit Eiffel-type wind tunnel in which the measured free-stream turbulence intensity is 0.16%. The zero-pressure-gradient boundary layer develops over a smooth, flat plate with width greater than ten times the greatest boundary-layer thickness to minimize side effects. The layer is tripped with a 4.7 mm diameter rod laid flat on the plate at $x = 110$ mm in the high-Reynolds-number case and $x = 1520$ mm in the low-Reynolds-number case. Measurements with and without the trip (Adrian *et al.* 2000*b*) reveal no differences in structure. The centre of the measurement volume is located at $x = 5310$ mm from the leading edge. The performance of the facility is documented in AMT; the layer is shown to be two-dimensional, with first- and second-order statistics in good agreement with established results. A thorough description of the facility is given in Meinhart (1994).

Two Reynolds numbers are considered, $Re_\theta = \theta U_\infty/\nu = 1015$ and 7705, where θ is the momentum thickness, U_∞ the free-stream velocity, and ν the air kinematic viscosity.

Re_θ	1015	7705
Re_δ	8743	61863
U_∞ (m s^{-1})	1.77	11.39
δ (mm)	76.2	83.1
θ (mm)	8.84	10.35
δ*(mm)	12.3	14.4
u_τ (m s^{-1})	0.086	0.41
y^* (mm)	0.179	0.0375
δ^+	426	2216
$H(\delta^*/\theta)$	1.391	1.391
θ/δ	0.116	0.125

TABLE 1. Smooth-wall boundary layer flow parameters.

Case	Recording medium	Re_θ	y^+	y/δ	Field of view $x/\delta \times z/\delta$	Field of view $x^+ \times z^+$	Number of realizations
LoH1	CCD	1015	21	0.05	1.08 × 2.55	460 × 1085	201
LoH2	CCD	1015	46	0.11	1.08 × 2.55	460 × 1085	201
LoH4	CCD	1015	92	0.22	1.08 × 2.55	460 × 1085	201
HiH1	CCD	7705	100	0.045	1.4 × 2.75	3100 × 6090	201
HiH2	CCD	7705	220	0.10	1.4 × 2.75	3100 × 6090	201
HiH3	CCD	7705	330	0.15	1.4 × 2.75	3100 × 6090	201
HiH4	CCD	7705	440	0.20	1.4 × 2.75	3100 × 6090	201
LoH1film	Film	1015	21	0.05	2.7 × 3.5	1150 × 1490	44
HiH1film	Film	7705	100	0.045	2.25 × 2.55	4980 × 5650	28
HiH4film	Film	7705	440	0.2	2.5 × 3.15	5540 × 6980	45

TABLE 2. Smooth-wall x–z plane measurement parameters.

The experiment is designed to closely match two sets of (x–y)-plane measurements in AMT. Table 1 shows several relevant flow parameters for the two cases.

2.2. *Measurement*

Two-dimensional velocity measurements are obtained in horizontal planes at several y locations using both digital and film PIV. Relevant measurement parameters are summarized in table 2. A complete set of digital data is obtained with wide spanwise view; this represents the foundation of the measurements, and the large number of samples in each case permits both quantitative and qualitative analysis. All statistics are based on these digital measurements. Additional data are obtained at a few selected heights of interest using film PIV. While the digital measurements are designed to capture a large spanwise view for this study, structures in wall turbulence are often large in both x and z, and visualization of entire structures requires wide-view measurement in both directions. The resolution offered by large-format film PIV makes such measurements possible. The difficulties associated with film PIV, however, effectively restrict the number of realizations per data set; thus, these measurements are used primarily for quantitative flow visualization.

The digital measurement heights extend from the near-wall region to the top of the logarithmic layer. Comparison between Reynolds numbers is possible at several heights, where y/δ is approximately 0.05, 0.1, and 0.2. The measurement heights for the film-based PIV are each selected for a specific purpose. The low-Reynolds-number,

Case	Δx^+	Δz^+	Δy^+	Number of vectors
LoH1	14	11	2.8	19 980
LoH2	14	11	2.8	19 980
LoH4	14	11	2.8	19 980
HiH1	60	48	13	24 750
HiH2	60	48	13	24 750
HiH3	60	48	13	24 750
HiH4	60	48	13	24 750
LoH1film	6	6	2.8	46 740
HiH1film	58	58	13	34 850
HiH4film	53	53	13	55 400

TABLE 3. Measurement volume dimensions.

near-wall ($y^+ = 21$) measurement height intersects the low-speed streaks. The lowest high-Reynolds-number measurement height ($y^+ = 100$) intersects relatively young packets growing along the wall, and the $y/\delta = 0.2$ measurements intersect mature vortex packets (based on observations in the (x–y)-plane; these packets typically extend up to $y/\delta = 0.4$–0.6).

Digital images are captured using two 2k by 2k CCD cameras set side-by-side, giving a 2:1 spanwise–streamwise view aspect ratio. Film measurements are captured with large-format 4 in. by 5 in. T-MAX 400 photographic film. Olive-oil particles of nominal 1–2 micron diameter are produced with an array of laskin nozzles (Griffin *et al.* 1973) and introduced passively upstream. The lasers and light-sheet forming optics are described in Tomkins & Adrian (2003). The time between pulses was set at 300 μs and 100 μs for the low and high Reynolds number, respectively, resulting in average particle image displacements in the range 11–15 pixels.

2.3. *Interrogation*

The double-exposed digital images are interrogated using single-frame cross-correlation with a discrete window offset specified *a priori*. The interrogation is carried out using PIV Sleuth software (Christensen, Soloff & Adrian 2000). No image shifting is necessary at these locations in this zero-pressure-gradient layer; the velocities never approach zero. Slightly rectangular spot sizes are used for the first window to improve resolution in the spanwise direction. The particle image diameter, d_τ, is typically 3–4 pixel diameters, giving d_τ/d_{pix} sufficiently large to minimize bias errors due to image discretization (Adrian 1997; Westerweel 1997). Peak fitting is done using a Gaussian 3-point estimator. The measurement volume in the fluid is defined by the interrogation spot size in x and z and the light sheet thickness in y. The velocity estimate is an average over this volume (Adrian 1988). The digital and film measurement volume parameters are summarized in table 3. Fifty percent overlap of interrogation spots yields digital measurement resolution of $5.6z^*$ by $7x^*$ at the low Reynolds number, and $24z^*$ by $30x^*$ at the high Reynolds number (x^* and z^* are viscous lengthscale units in the streamwise and spanwise directions, respectively). The above procedure yields approximately 20 000 and 25 000 vectors at the low and high Reynolds number, respectively, with a low percentage of obviously spurious measurements. The raw fields are validated by systematic removal of bad vectors and replacement with 2nd and 3rd choices in the correlation plane where appropriate. One pass of interpolation given a high percentage of neighbouring valid measurements is performed, and finally a narrow Gaussian filter is applied to remove spatial high-frequency noise.

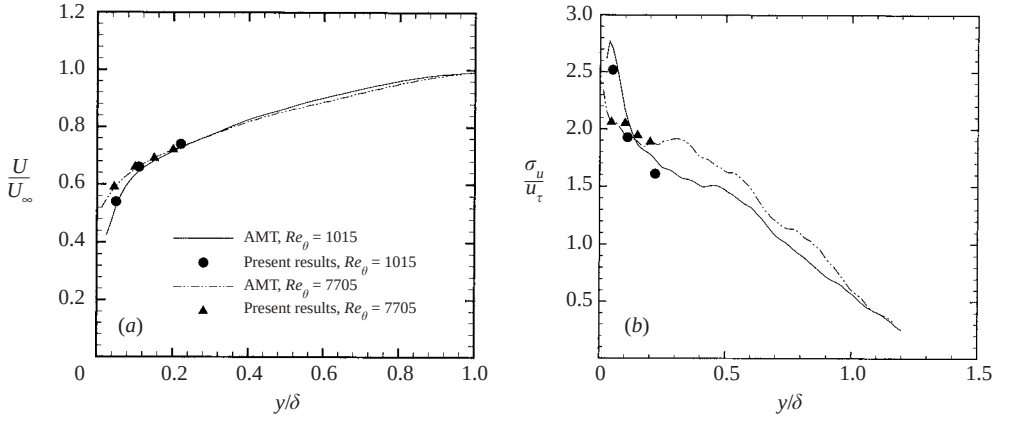

FIGURE 1. (*a*) Mean streamwise velocity versus wall-normal location, scaled and plotted in outer units; (*b*) root-mean-square streamwise velocity versus wall-normal location, scaled in inner units, plotted in outer units. Comparison with AMT.

The film data are interrogated by back-illuminating individual negatives with incoherent light, then scanning the whole area section-by-section using a Videk Megaplus 1024×1024 CCD camera and processing individual sections. Sections are interrogated using a single-frame, double-exposure, cross-correlation algorithm (implemented by Christensen 2000). Raw velocity information is then post-processed, with invalid measurements being removed using Cleanvec software (Meinhart 1994; Soloff 1998) in a procedure similar to the one for the digital data.

With velocity bias error minimized by the cross-correlation interrogation procedure, the principle error of the measurement is the random error in the peak estimation. Prasad *et al.* (1992) calculate this error to be in the range $0.05d_\tau$–$0.1d_\tau$. Thus, the displacement error is approximately 0.25 pixels, which corresponds to roughly 1.1% of the free-stream velocity.

2.4. *The boundary-layer flow field*

Statistical quantities are calculated by ensemble averaging over all realizations and then averaging streamwise and spanwise. Figure 1(*a*) shows mean streamwise velocity at each height plotted in outer units against the mean velocity profile measured in AMT for each Reynolds number. Good agreement is found for both cases. As the top of the logarithmic region is approached all four sets of data converge, as expected. In figure 1(*b*) fluctuating streamwise velocity is plotted for both Reynolds numbers against the x–y data; again agreement is good, particularly at the higher Reynolds number. The low-Reynolds-number (x–z)-plane measurements are slightly below the (x–y)-plane curve. This difference may be a manifestation of the limited resolution of the data in the highly turbulent near-wall region. The points are within the sampling error of the (x–y)-plane measurements for second-order statistics, however.

3. Large-scale structure

Investigations of boundary-layer structure at moderately high Reynolds number ($Re_\theta > 6000$ or so) reveal large-scale structures inclined from the wall at a relatively shallow angle, in the range 10°–20°, as viewed from the (x–y)-plane (Head & Bandyopadhyay 1981; Brown & Thomas 1977; AMT). These structures extend

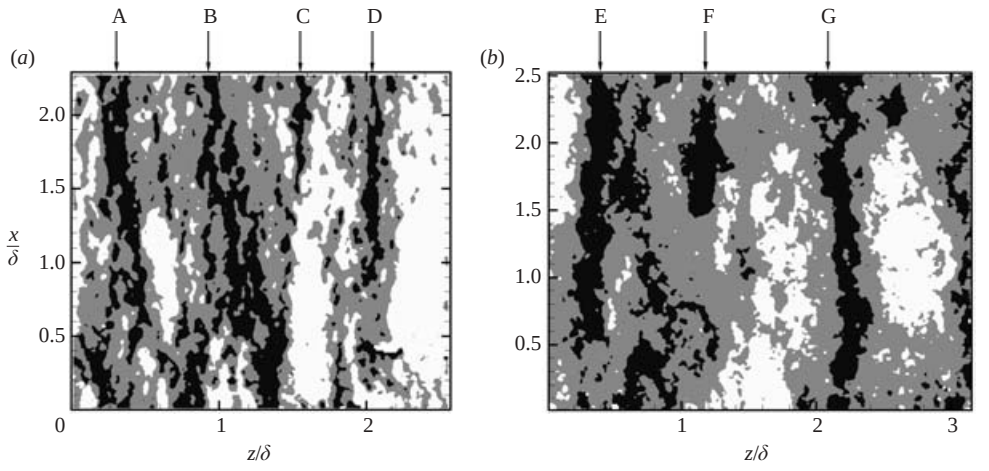

FIGURE 2. Instantaneous u-velocity contours revealing elongated low-momentum regions at $Re_\theta = 7705$. Black region, 10% below local mean; white region, 10% above local mean. (*a*) $y^+ = 100$, $y/\delta = 0.045$; (*b*) $y^+ = 440$, $y/\delta = 0.2$.

through the logarithmic region, so the measurement volume in the present study will intersect these structures in various stages of evolution. Careful inspection of numerous instantaneous realizations at each y location at $Re_\theta = 7705$ reveals that the dominant large-scale structures are regions of low-momentum fluid, highly elongated in the streamwise direction. These low-momentum regions (LMRs) are visible at every wall-normal location in table 2 at the high Reynolds number. They are distinct from the near-wall low-speed streaks, often extending 500 viscous wall units spanwise or more.

Examples of these LMRs at approximately the bottom and top of the logarithmic region are given in figure 2. Contours of streamwise velocity are plotted, with dark regions corresponding to lower-speed fluid and white regions higher-speed fluid. Each realization contains 3 to 4 examples of these structures, marked A to G. These examples are representative of the LMRs in the data, although not every realization contains 3 to 4 clear examples. The wall-normal location is reflected in the structure. At $y/\delta = 0.2$, figure 2(*b*), the LMRs are more uniform, and fewer small-scale regions are visible. Closer to the wall, figure 2(*a*), the continuity of the regions is reduced, consistent with the increased fluctuations near the wall. Also, more small-scale regions, such as C and D, appear at $y^+ = 100$. This observation is consistent with the attached-eddy hypothesis (Townsend 1976), in the sense that both large- and small-scale motions are expected to contribute closer to the wall.

3.1. *Properties of the low-momentum regions*

The spanwise size of the large scales is estimated at each height by measuring the width of the low-speed regions along a spanwise 'slice' of the data at the streamwise midpoint of each realization. (Here 'low speed' is defined as less than 90% of the local mean.) Each width is recorded and binned to obtain a distribution of widths as a function of distance from the wall, presented in figure 3. Two trends are apparent. First, the mean streak width and most probable streak width increase with distance from the wall. This demonstrates the growth of the spanwise scales throughout the logarithmic region. Secondly, the distribution of streak widths decreases with distance from the wall relative to the mean width.

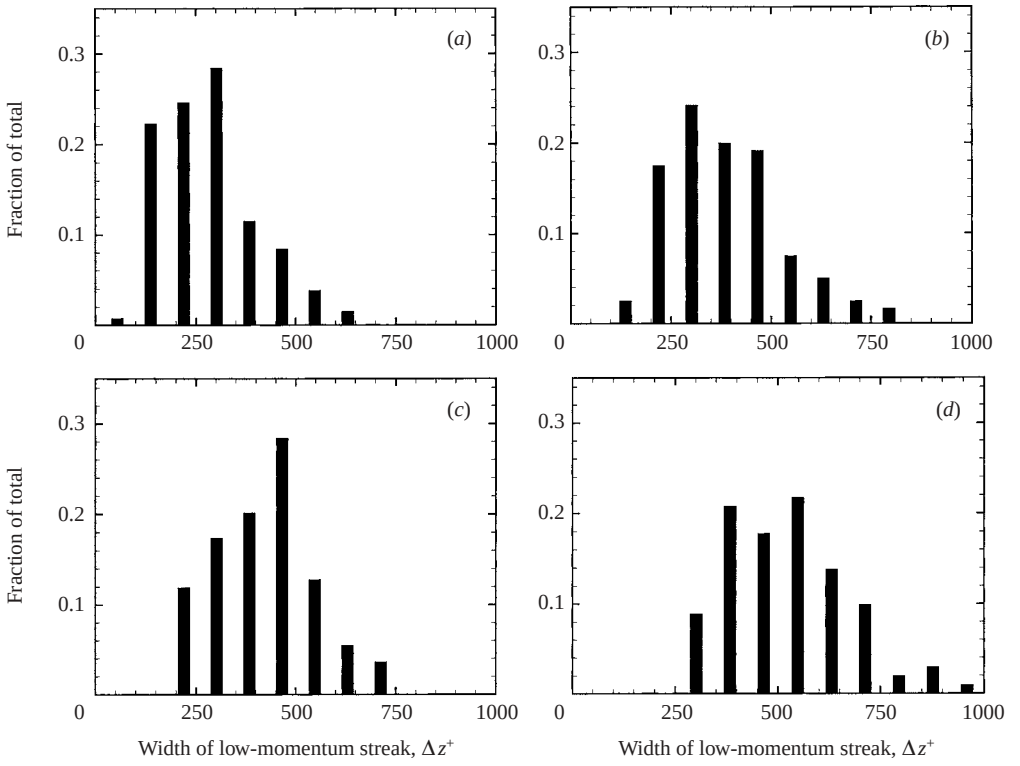

FIGURE 3. Histograms of spanwise size of low-speed regions at $Re_\theta = 7705$. (*a*) $y^+ = 100$; (*b*) $y^+ = 220$; (*c*) $y^+ = 330$; (*d*) $y^+ = 440$.

The mean spanwise width is plotted against wall-normal location in figure 5(*a*) below (black squares). The size of the structures varies almost linearly with distance from the wall, consistent with the attached-eddy hypothesis and self-similar growth of the structures. This is the first of several spanwise lengthscales shown to exhibit linear growth. The other symbols in the figure are discussed shortly.

Streamwise properties are more difficult to estimate due to the long streamwise extent of the motions. Even using the long-streamwise-view film results, estimates are not reliable, because the extent of the structure is often close to the view extent, resulting in significant bias against longer structures. However, a range of sizes may be estimated based on instantaneous realizations at the top and bottom of the logarithmic region. As seen in figure 2(*b*), at $y/\delta = 0.2$ structures may extend 2δ–2.5δ streamwise in the plane (e.g. E and G). Of course younger, smaller structures are also growing and 'poking through' the plane from below. The intersection of these structures with the measurement volume will reveal much smaller areas of momentum deficit as well. At $y^+ = 100$ similar behaviour is observed. The largest structures will extend the entire streamwise view, 2δ–2.5δ, and much shorter structures are also present. These estimates of the structural dimensions compare well with the conditional results of Wark & Nagib (1991). Also, the quasi-periodicity Wark & Nagib discuss is apparent in the present data; the instantaneous fields often reveal regions of high momentum between the low-speed structures.

Thus, the instantaneous realizations reveal the dominant structures and permit estimation of their properties. Quantitative confirmation of their frequency and

contribution to the flow field is necessary, however; this may be obtained with conditional averaging.

3.2. *Linear estimate of a low-momentum event*

Linear stochastic estimation (Adrian 1975) is a means of estimating conditional averages of a process with unconditional data. The stochastic estimate of u_i given some event E_j is

$$\langle \hat{u}_i | E_j \rangle = A_{ij} E_j + B_{ijk} E_j E_k + \ldots . \tag{3.1}$$

The coefficients A_{ij} and B_{ijk} are estimated by minimizing the mean-square error of the estimate. If the estimate is linear, only the first term on the right is retained.

Here linear stochastic estimation (LSE) will be used to estimate the conditional velocity field $\langle u_i(\boldsymbol{x}+\boldsymbol{r}) | \boldsymbol{u}(\boldsymbol{x}) \rangle$ given a negative-u_1 event. For the case of only one event component specified, the linear estimate reduces to

$$\langle \hat{u}_i(\boldsymbol{x}+\boldsymbol{r}) | u_1(\boldsymbol{x}) \rangle = L_{i1} u_1(\boldsymbol{x}) \tag{3.2}$$

with $i = 1, 2$, and

$$L_{i1} = \frac{\langle u_1(\boldsymbol{x}) u_i(\boldsymbol{x}+\boldsymbol{r}) \rangle}{\langle u_1^2 \rangle}. \tag{3.3}$$

Estimates are obtained at each y location. Velocity vector plots of the estimates reveal that the average structure, given an event of negative fluctuating streamwise velocity, is a large region of low streamwise momentum elongated in x, completely consistent with the observations from the instantaneous realizations. The size and shape of the conditional velocity field are readily revealed with contours of streamwise velocity (see figure 4). The negative event corresponds to minus one standard deviation of u_1. The spanwise and streamwise dimensions of the low-speed area increase with distance from the wall. Lower level contours, such as -0.2 or -0.3, show little variation with the streamwise coordinate, suggesting that the motions extend well beyond the streamwise view of 2000 viscous wall units.

The average properties of the conditional structure may be estimated using higher level contours. Figure 5(*a*) shows lengthscales based on the extent of the -0.4 contour in x and z plotted versus distance from the wall, along with the earlier spanwise lengthscale estimate from the histograms of streak width. The spanwise width of the average structure shows linear variation with y, and remarkable agreement with the earlier histogram-based estimate; both exhibit Townsend's 'attached-eddy' behaviour. The streamwise length of the streaks shows some scatter with respect to the linear fit; it appears to level off as the outer region is approached. The streamwise:spanwise aspect ratio is plotted in figure 5(*b*) using both LSE-based scales. Structures are more elongated close to the wall, with aspect ratio near 6, and become less elongated further from the wall, with aspect ratio near 4. Tomkins & Adrian (2003) estimated the aspect ratio of energy-containing structures using the median energetic wavelength with corroborating results. Krogstad & Antonia (1994) also observed a similar trend with correlation-based lengthscale measurements. Thus, the observations from the instantaneous realizations are supported by the linear stochastic estimate. These low-momentum regions are shown to occur so frequently as to dominate the conditional average, and estimates of their average spanwise growth from quantitative visualization are in excellent agreement with the spanwise growth of the conditional average.

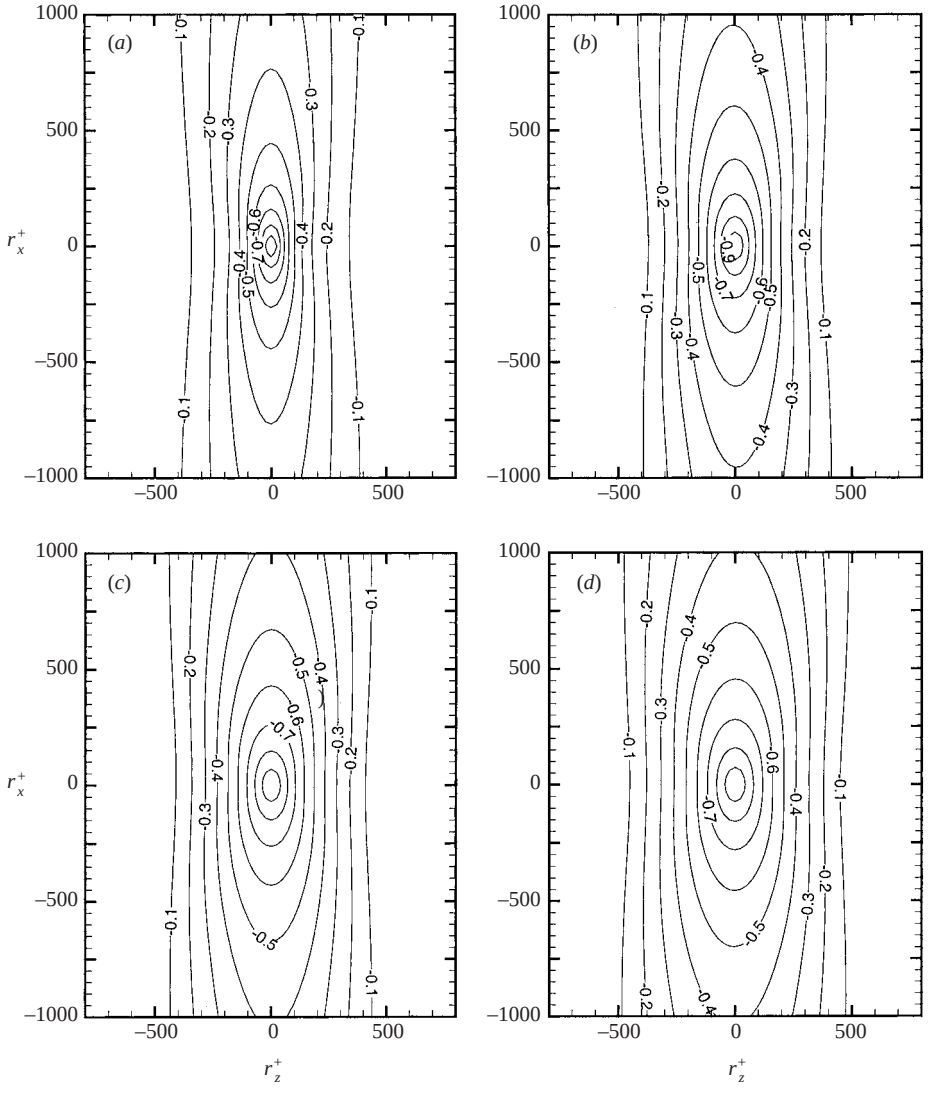

FIGURE 4. u-contours of the single-point linear stochastic estimate given a negative-u event at $Re_\theta = 7705$. (*a*) $y^+ = 100$; (*b*) $y^+ = 220$; (*c*) $y^+ = 330$; (*d*) $y^+ = 440$.

4. Association of the small with the large scales

Having identified the dominant large-scale structures and examined their properties, we now address the question of how are they are created. AMT observe ramp-like structures in (x–y)-plane data that are consistently associated with spanwise vortices. The authors hypothesize that the large-scale structures are created by the cooperative induction of a series of streamwise-aligned hairpin-type vortices. The intersection of the vortex heads with the measurement volume creates the observed spanwise vortices. The idea that the small scales work cooperatively to create the large scales is an interesting and important aspect of the vortex packet model. In this section we investigate the relation of the small scales to the much larger scales, and educe the dominant small-scale structure of the flow.

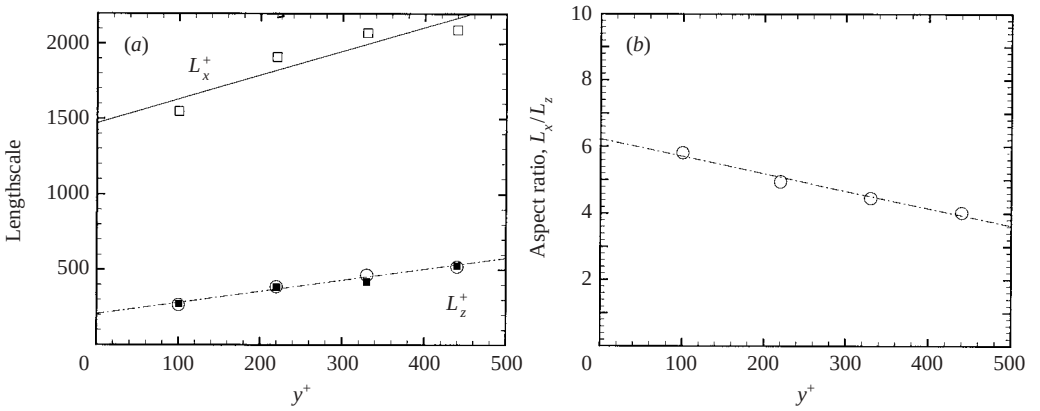

FIGURE 5. (*a*) Streamwise and spanwise lengthscales versus y-location at $Re_\theta = 7705$. □, streamwise lengthscale L_x based on u-contours of LSE given negative-u event; ○, spanwise lengthscale L_z based on u-contours of LSE given negative-u event; ■, spanwise lengthscale based on mean width of streaks. (*b*) Streamwise:spanwise aspect ratio, L_x/L_z, versus y-location.

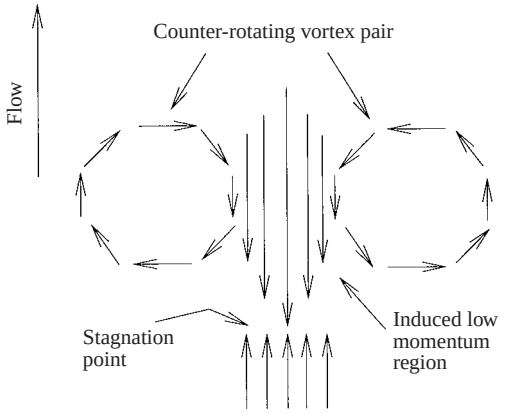

FIGURE 6. Idealized streamwise–spanwise hairpin vortex signature.

4.1. *Hairpin vortex signature*

An important step in the analysis of AMT was the identification of the velocity vector pattern created when the measurement volume slices between the legs of a hairpin-type vortex, defined as the *hairpin vortex signature* (HVS). AMT successfully used this pattern in identifying hairpin-type vortices in the data. Similarly, a vortex signature may be defined in the (x–z)-plane. An idealized signature consists of two principle components: (i) two elliptical counter-rotating vortex patterns created by the intersection of the light sheet with the angled vortex legs, and (ii) a low-u-momentum event created by the backwards induction of the legs and the vortex head. A third element of the signature may also appear, a stagnation point created at the interface between the induced low-momentum event and faster upstream fluid. A schematic of an idealized (x–z)-plane hairpin vortex signature is shown in figure 6. The vortex legs (here depicted as roughly circular), the induced low-u-momentum event, and the stagnation point are labelled. The elliptical shape of the legs is a consequence of the

intersection of the horizontal light sheet with the angled vortex legs. The size of the major and minor axes of the ellipse, of course, will vary with the size and angle of the vortex at that y location. Because the angle of inclination of the vortices is observed to increase with distance from the wall, the $(x–z)$-plane HVS varies as a function of y as well.

Within a highly turbulent flow, of course, each vortex is formed under unique conditions and subject to a variety of influences during its evolution. Hence, no two vortices will be identical, and no two associated $(x–z)$-plane vector patterns will be identical. Several authors have noted that one-legged hairpins or cane-like structures occur more frequently than two-legged hairpins (Guezennec, Piomelli & Kim 1987; Robinson 1991). Asymmetric hairpins with one dominant leg may also occur. In these cases, only one elliptical vortex leg might appear in the signature, and the associated low-speed region might also have a degree of asymmetry. These and related patterns are all considered signatures of hairpin-type vortices.

Examples of HVS in the instantaneous data are given in figure 7 at three different wall-normal locations with $Re_\theta = 1015$. The low-Reynolds-number results offer increased resolution of the signatures, and measurements deeper in the boundary layer. Velocity vectors are plotted with a constant convection velocity, U_c, subtracted (Galilean decomposition) as discussed in detail in AMT and Adrian, Christensen & Liu (2000*a*). This type of decomposition is used throughout the present paper, and when viewing data in the horizontal plane, it is equivalent to Reynolds decomposition if U_c is the local mean. In figure 7, U_c is roughly equal to the speed of the vortex in each case, and flow is from bottom to top. In each example the elements of the HVS are present: counter-rotating vortices border induced low-speed regions. Ellipses have been placed on the figure to mark the swirling velocity vector patterns. The aspect ratio of the patterns, and the marking ellipses, becomes closer to unity as distance from the wall increases, as the vortex legs become more vertically inclined. The sudden change in velocity characteristic of a stagnation point (when viewed in the appropriate reference frame) is present in figures 7(*b*) and 7(*c*) upstream of each vortex. This stagnation point may not be present if an additional vortex follows upstream, as the upstream vortex prevents the impingement of high-speed fluid on the low-speed region.

4.2. *Instantaneous fields*

The relationship between the large and the small scales is now investigated in the logarithmic region by close examination of instantaneous realizations. Several of the low-momentum regions identified in figure 2 are extracted and examined in detail. In figure 8, the structure labelled C in figure 2(*a*) is presented. Here, $Re_\theta = 7705$ and the measurement volume intersects approximately the bottom of the log layer ($y^+ = 100$, $y/\delta = 0.045$). Figure 8(*a*) shows velocity vectors with $U_c = 0.65U_\infty$ and flow bottom to top, so that downward vectors represent low-speed fluid. Careful inspection of the plot reveals that the elongated low-momentum region is actually a series of $(x–z)$-plane vortex signatures, closely spaced and aligned roughly streamwise. At the higher Reynolds number, the vortex signatures are not as well resolved as in the low-Re data, due to the diminishing viscous lengthscale of the flow. The key elements of the signatures are present, however, and in abundance. Approximately 15 structures with vertical swirling motion are visible. Circles are placed on these structures, by hand, for identification, and labels are attached to many. Several of these structures appear to be counter-rotating vortex pairs, including A1/A2, C1/C2, and D1/D2; these

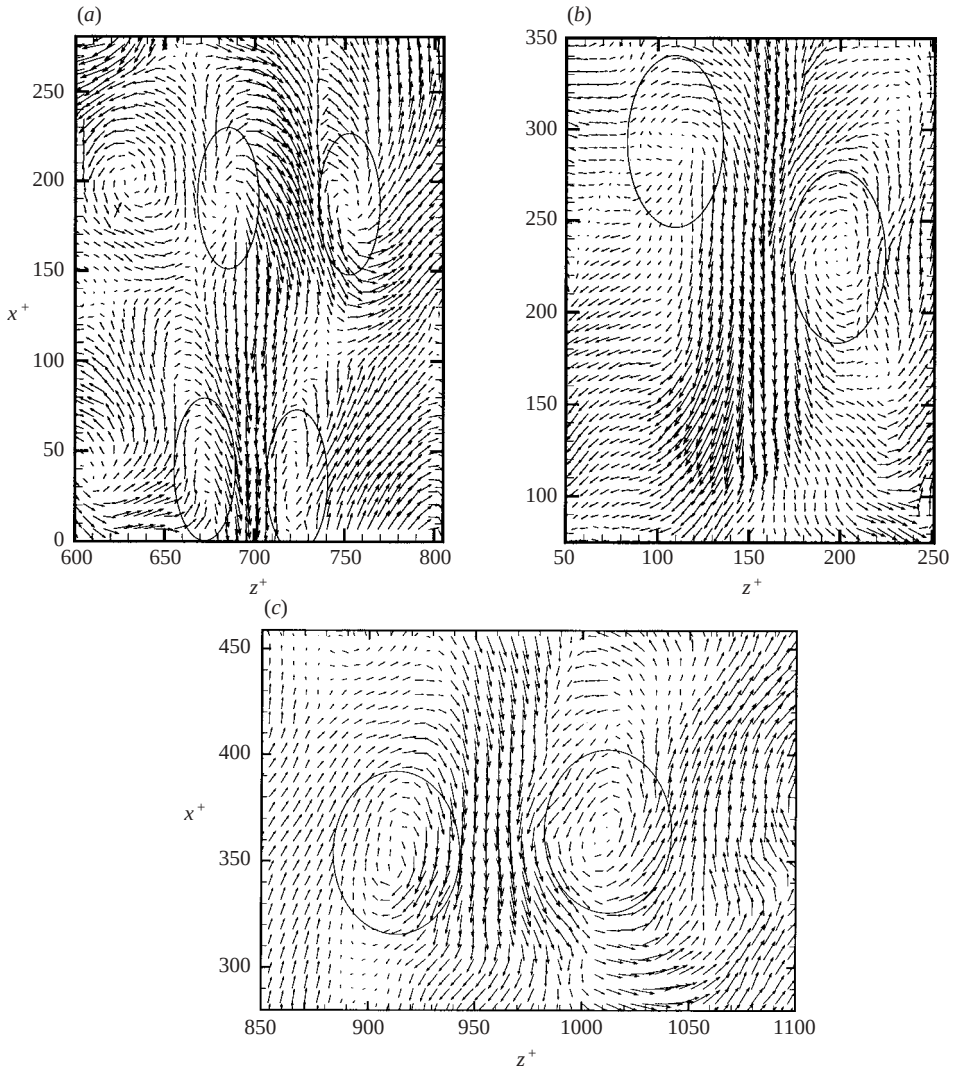

FIGURE 7. Hairpin vortex signatures in the (x–z)-plane as a function of y. (a) $y^+ = 21$; (b) $y^+ = 46$; (c) $y^+ = 92$.

patterns are consistent with the presence of two-legged hairpin-type vortices. Other structures (e.g. F, G, and J) are one-sided vortex signatures. The cumulative effect of these structures is a long, thin region of momentum deficit. The sinuous nature of the region is a consequence of the asymmetry and imperfect alignment of the vortices. Although these structures appear to be relatively young, by virtue of their width, the region extends nearly 1.5δ streamwise, which corresponds to over 3000 viscous wall units.

Adrian *et al.* (2000*a*) investigated vortex visualization with velocity vector plots. The authors concluded that if a velocity vector pattern with roughly circular streamlines appears when using Galilean decomposition, then not only does a vortex exist at that location, but that vortex is moving at approximately the decomposition convection velocity. The implication of this result for the present study is that not only do

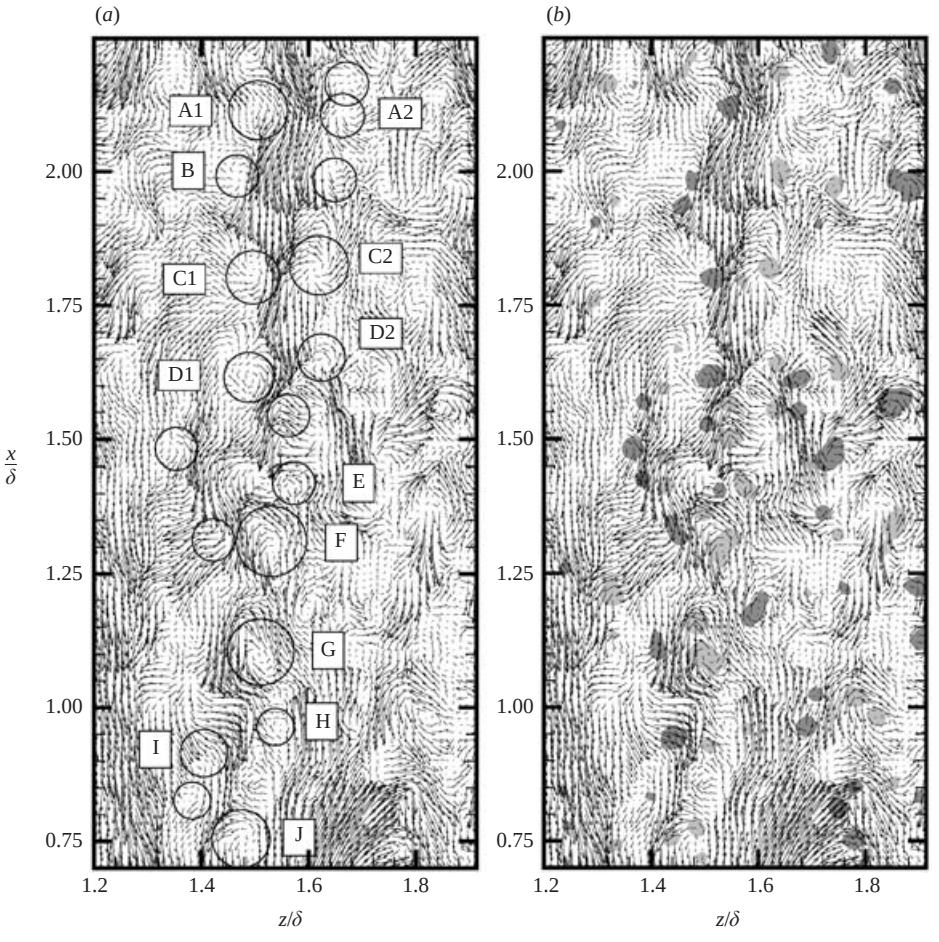

FIGURE 8. Instantaneous field at $y^+ = 100$ and $Re_\theta = 7705$: structure C in figure 2(a). (a) Velocity vectors with vortices circled, $U_c = 0.65U_\infty$; (b) velocity vectors with patches of $\lambda_{ci}\omega_y/|\omega_y|$. Light grey patches represent counter-clockwise rotation, dark grey represents clockwise rotation.

the vector patterns identified in figure 8(a) represent vortices, but those vortices are convecting at roughly the same velocity. Thus, the structures are propagating downstream together with little dispersive velocity.

The same structure appears in figure 8(b), with patches of $\lambda_{ci}\omega_y/|\omega_y|$ plotted under the velocity vectors. λ_{ci}, or swirling strength, is the imaginary part of the complex eigenvalue of the velocity gradient tensor. It is shown by Zhou *et al.* (1999) and Adrian *et al.* (2000a) to be an effective vortex identification tool. λ_{ci} captures the local swirling character of a region without contamination from shear (unlike vorticity). Here it is multiplied by the sign of the vertical vorticity to capture the direction of swirl at each point. Light grey patches represent counter-clockwise rotation ($\omega_y < 0$) and dark grey represents clockwise rotation ($\omega_y > 0$).

The swirling strength contours quantitatively verify the existence of the vortices identified in figure 8(a). The sign of rotation is consistent with the hypothesis that the streak is a consequence of vortex induction: counter-clockwise vortices generally appear on the right of the low-speed streak, and clockwise vortices appear on the

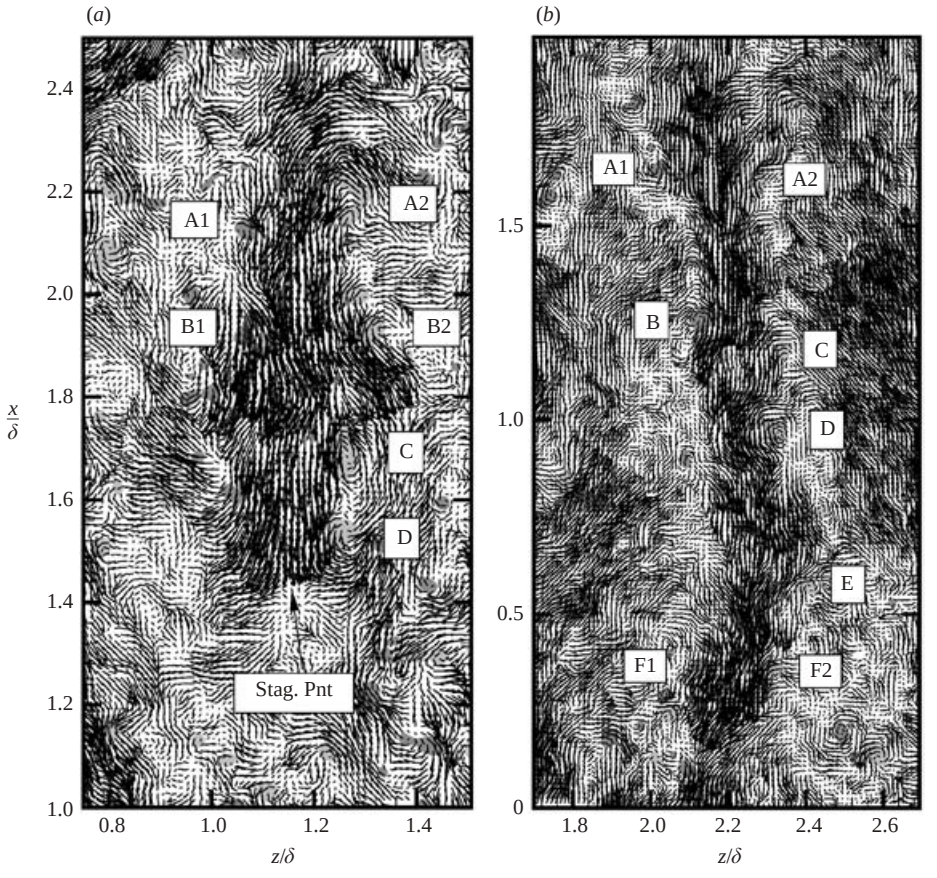

FIGURE 9. Instantaneous velocity vector fields with patches of $\lambda_{ci}\omega_y/|\omega_y|$ plotted at $y/\delta = 0.2$ and $Re_\theta = 7705$. (*a*) Structure F in figure 2(*b*); (b) structure G in figure 2(*b*).

left. The technique also extracts additional structures not immediately obvious from the vector plot, many of which border the low-momentum region. Differences in the convection velocities of vortices can create subtle differences in their appearance in a decomposed velocity vector field, thereby masking their presence. The swirling strength analysis is invariant with respect to the convection velocity, and therefore effective in extracting all of the vortical structures. It confirms the close association of swirling regions with the low-momentum streak.

The results in figure 8 provide a strong instantaneous link between the large and small scales. The high density of HVS (in this and other realizations) suggests that one- and two-legged hairpin vortices occur frequently at this Reynolds number. Furthermore, several aspects of the data offer strong support for the vortex packet model of AMT, including: (i) the streamwise alignment of these vortex signatures; (ii) the long, sinuous region of momentum deficit they appear to induce; and (iii) the appearance of a high percentage of vortices in the group at a single convection velocity.

The above results are found near the bottom of the logarithmic region. Structures at the top of the log layer ($y/\delta = 0.2$, $y^+ = 440$) are now examined. Again the large structures first identified in figure 2 are presented; the structures labelled F and G are plotted in figures 9(*a*) and 9(*b*), respectively. In these older, larger structures, the

individual vortex signatures, while visible upon close inspection, are not as obvious as in the previous near-wall example, as the induced low-speed regions appear to overlap to form a roughly continuous LMR. Hence, contours of $\lambda_{ci}\omega_y/|\omega_y|$ are relied on as the primary vortex identification tool.

Many similarities exist with the structure at $y^+ = 100$. The contours reveal numerous vortices in each example: approximately 12 in figure 9(a) and 20 in 9(b). As before, several of these are paired (e.g. A1/A2 and B1/B2 in 9(a); A1/A2 and F1/F2 in 9(b)), and many of these appear to be unpaired (e.g. C and D in 9(a); B, C, D, and E in 9(b)). Careful inspection of these vortices reveals swirling velocity vector patterns, and the sign of the swirl is such that the associated rotation will enhance the low-momentum streak. Note also the stagnation point appearing upstream of the final vortex in figure 9(a), vortex D. In each case, the vortices are aligned streamwise with a remarkable degree of coherence considering the significant background level of turbulence. The structure in figure 9(a) will perhaps extend further streamwise underneath this plane; its relatively abrupt starting and ending points give the impression that it is 'poking through' the plane from below. The structure in figure 9(b) extends 2δ or so streamwise in this plane, equivalent to over 4000 viscous wall units.

While the basic characteristics of large- and small-scale structure appear similar at both ends of the log layer, some differences do appear farther from the wall. For example, the spanwise size of the structures is greater than in the earlier case, as expected with the increasing spanwise lengthscales. Also, the percentage of vortices paired with a counter-rotating structure reduces farther from the wall; perhaps this is a manifestation of the disrupting influence of the turbulence on the older flow structures. Quantitative verification of this decrease in symmetry is provided subsequently.

The foregoing examples provide strong supporting evidence for the idea that hairpin-type vortices organize to create large-scale, elongated regions of momentum deficit. It is necessary, however, to comment on the frequency with which such examples occur in the data. The above structures may be considered 'good examples' of vortex packets: they exhibit a slightly higher degree of organization than the typical structure, and the vortex swirling motions are consistently clear. However, these realizations were not selected because they contained one or two 'ideal' examples, but because they each contain several elements that are characteristic of the ensemble of data. The presented structures, then, are far from unusual, and the typical structure at each height *does* exhibit the features embodied in these examples: at $y^+ = 100$, young, thinner structures typically contain several one- or two-legged vortex signatures, and these signatures are roughly aligned streamwise; at $y/\delta = 0.2$, older, wider structures are almost always associated with a series of one- or two-sided vortices. Inspection of digital data at the other heights throughout the logarithmic region ($y^+ = 220$, 330; $y/\delta = 0.1$, 0.15) reveals similar patterns.

The idea that the boundary layer contains a hierarchy of vortices has been suggested by several researchers (e.g. Perry & Chong 1982). The present data provide an alternative (i.e. streamwise–spanwise) perspective on this idea. Structures like the larger, older ones presented in figure 9 at $y/\delta = 0.2$ extending down to the near-wall region would explain the large energy found near the wall in the streamwise power spectrum at wavelengths λ_z^+ significantly greater than 100 (Liu, Adrian & Hanratty 1996; Tomkins & Adrian 2003). Their presence there, amidst younger, growing structures, may be expected to have interesting effects. One effect that may be conjectured with some certainty is an increase in flow complexity. In such a case, further analysis may be required to educe the dominant structure.

4.3. *Filtered fields*

At higher Reynolds number the range of scales in the flow increases. Low-pass filtering the data helps in visualizing the flow structure. In the present results, filtering in the spanwise direction is employed in an attempt to separate the near-wall, smaller-scale streaky structures from the large scales. The filtering is implemented by Fourier transforming the data, performing a sharp, low-pass cutoff in Fourier space, and transforming back to physical space. The spanwise filter $G(k)$ is defined in Fourier space as

$$G(k) = \begin{cases} 1, & |k| < k_c \\ 0, & |k| \geqslant k_c. \end{cases}$$

The filter cutoff, k_c, corresponds to a wavelength of $\lambda_{z,c}^+ = 500$, chosen because the spanwise spacing of streaky structures at $y^+ = 100$ is determined by flow visualization to be approximately $\lambda_z^+ = 500$ (Kasagi 1988). The fluctuating field is the difference between the total field and the filtered field.

Filtering is particularly effective when visualizing flow patterns with a wide range of scales. The realization in figure 2(*a*), in addition to providing clear examples of relatively young vortex packets (C and D), provides examples of larger, presumably older, structures (A and B). Casual inspection of these larger structures does not reveal the clear HVS and organization observed in structure C (figure 8). For example, the wide region of low-speed fluid labelled A in figure 2(*a*) contains numerous small-scale fluctuations visible to the eye, but without obvious interpretation.

The spanwise filtering procedure is applied to structure A, and both the large- and small-scale fields are presented in figure 10. Remarkably, the large-scale field reveals an elongated region of low-momentum fluid, bordered by numerous rotating velocity vector patterns. Circles are placed over the rotating patterns for identification; approximately 13 appear in this example. The earlier characteristics of the large-scale structures are now clear with the removal of the small-scale field: vortex signatures, both one- and two-legged; the alignment of the signatures roughly in x; and the stagnation point behind the upstream-most vortex. This structure is thus interpreted to be a slightly older, larger version of structure C in figure 2(*a*), i.e. a vortex packet. It has grown well through the $y^+ = 100$ measurement plane but is rooted near the wall. Its influence is clear from the contours of streamwise velocity, but its nature is masked in the total field by the high level of fluctuations.

Careful inspection of the fluctuations shown in figure 10(*b*) reveals numerous, perhaps 40–80, small structures with rotation in the wall-normal direction. Many of these have been circled. The vortices are observed to induce small-scale fluctuations in the data, both positive and negative, in both x and z. Examples of these induced fluctuations are labelled 'IF'. Miniature hairpin vortex signatures are also visible, though not always adequately resolved. Four examples are selected arbitrarily and labelled. Physical interpretation of the small-scale field is not as obvious as for the large-scale field; these motions may be young structures growing from the wall, fragments of disrupted structures, or vortices created locally by shear.

Structure 'A' is one example that contains the hierarchy of scales present near the wall in a high-Reynolds-number flow. Similar structures exist throughout the data, with multiple examples appearing in most wide-view realizations at $y^+ = 100$. In these motions, the filtering operation consistently reveals vortices, of relatively large scale, organizing to create a much larger scale.

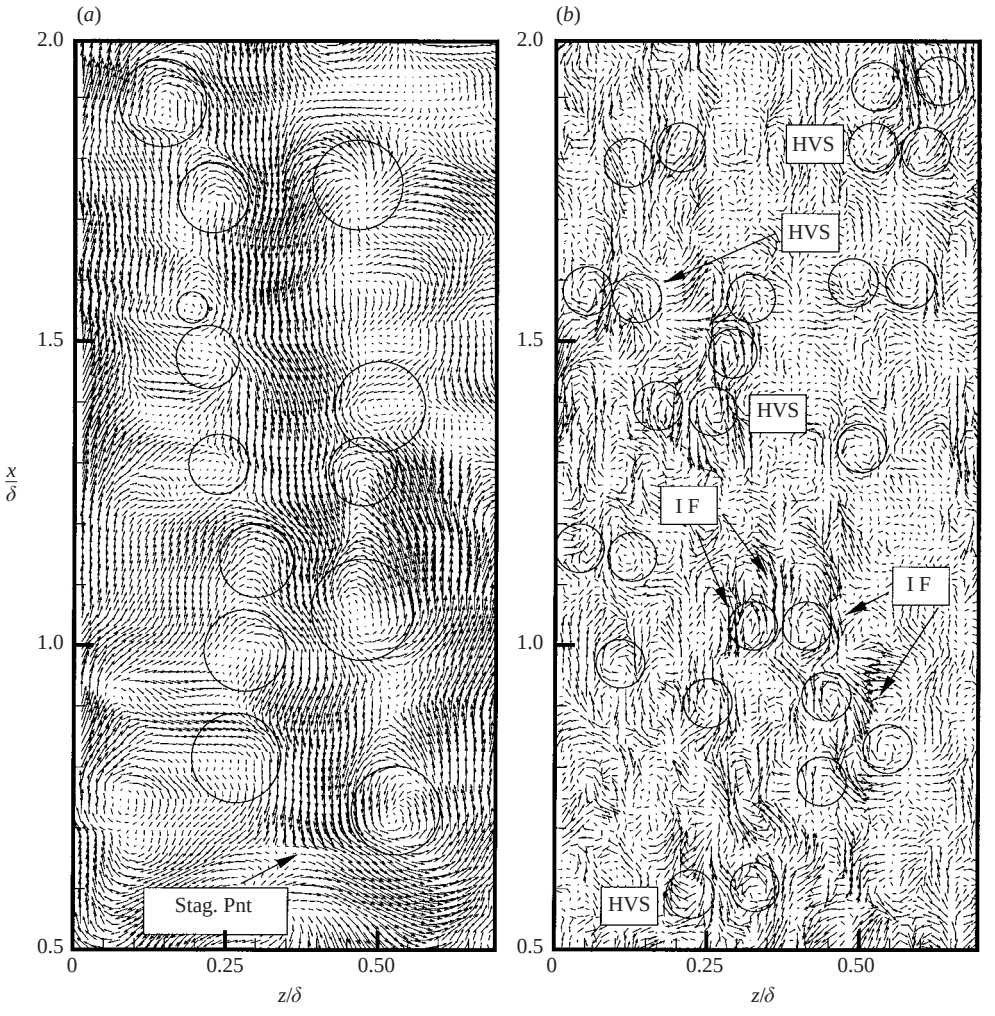

FIGURE 10. Low-momentum structure A in figure 2*a* filtered with $\lambda_{z,c}^{+} = 500$. (*a*) Large-scale field; (*b*) small-scale field.

In investigating these largest scales earlier, stochastic estimation was employed to quantitatively verify the existence and importance of the low-momentum structures. A similar approach is appropriate for the commonly observed structural units that are hypothesized to comprise these large scales.

4.4. *Conditional eddy*

The density of (x–z)-plane vortex signatures throughout the data strongly suggests that hairpin vortices occur frequently throughout the logarithmic region at elevated Reynolds number. Conditional averaging is employed here to educe the dominant small-scale structure. In examining the large-scale regions of low momentum, a negative u-event was specified; this averages over all low-speed events, and successfully extracts the dominant large-scale feature of the flow. Here, we are concerned with the smaller-scale, more local features of the flow. Accordingly, the conditional event must contain local information. The specification of a local minimum (i.e. a point at which the velocity is lower than any of the eight surrounding points) beneath some

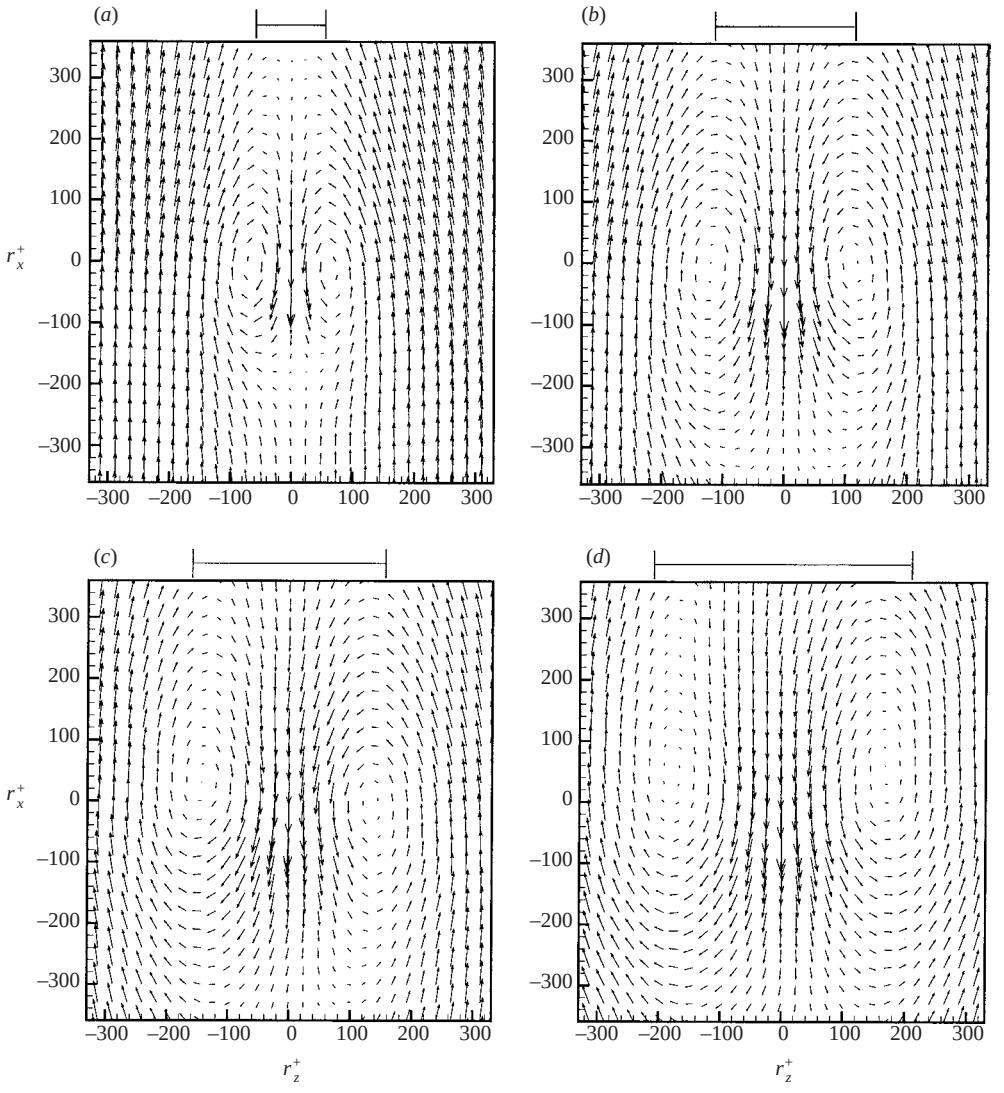

FIGURE 11. Conditionally averaged structure in the $(x–z)$-plane at $Re_\theta = 7705$. The specified event is a local u-minimum with $u < 0.75U_\infty$. (*a*) $y^+ = 100$; (*b*) $y^+ = 220$; (*c*) $y^+ = 330$; (*d*) $y^+ = 440$.

threshold captures the local character of the flow while ensuring that local minima in high-speed regions do not contribute to the average. The threshold here is set at 75% of the local mean velocity. Thus, the conditionally extracted structure based on this event represents the average structure associated with a local minimum in a region of low momentum.

This conditional eddy is plotted in figure 11 as a function of distance from the wall. The conditional structure bears a remarkable resemblance to the hairpin-vortex signature defined earlier. With only a u-based event specified (no spanwise component), a pair of counter-rotating vortices is extracted from the data at each height. As distance from the wall increases the legs become further apart, the vortex cores become thicker, and the elliptical shape of the streamlines becomes more

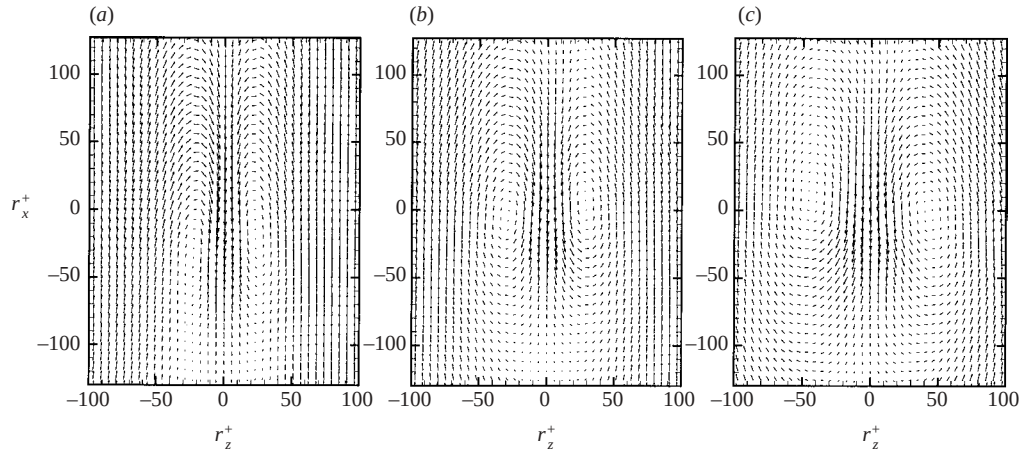

FIGURE 12. Conditionally averaged structure in the $(x–z)$-plane at $Re_\theta = 1015$. The specified event is a local u-minimum with $u < 0.75U_\infty$. (*a*) $y^+ = 21$; (*b*) $y^+ = 46$; (*c*) $y^+ = 92$.

circular. All of these observations are consistent with a hairpin-vortex interpretation. Furthermore, the persistence of the hairpin pattern through the average confirms (i) its importance in the flow, and (ii) its consistent association with regions of minimum streamwise velocity. An alternative interpretation of the latter point is that the hairpin is consistently associated with regions of maximum backwards induction. The symmetry of the pattern is simply a consequence of the statistical symmetry of the flow and of the specified event with respect to reflections about the $(x–y)$-plane; individual structures, of course, may be asymmetric to varying degrees. Thus, hairpin-type vortices are extracted as the dominant small-scale structure, confirming numerous observations in the data, and statistically linking the hairpin to the earlier observed large-scale structure.

5. Packets in the near-wall region

The preceding results provide evidence for the existence of hairpins and their association with low-momentum regions throughout the logarithmic layer at higher Reynolds number. In this section, evidence of a similar nature is presented for the region $y^+ < 60$, where the existence of hairpins (and organized hairpins) remains in dispute. Two sets of measurements in the $Re_\theta = 1015$ layer are performed in this region: $y^+ = 21$ and 46.

The $y^+ = 21$ measurements are designed to intersect the low-speed streaks, and indeed the streaks are the dominant structure at this height. Vortices with a significant component of vertical rotation are observed here, as in figure 7(*a*), but less frequently than in the results further from the wall. This is consistent with the observations in the literature of the quasi-streamwise vortex cores (hairpin legs) centred around $y^+ = 20–40$.

At $y^+ = 46$, however, vertically oriented vortices are very common. As expected, both single and counter-rotating pairs exist, typically in close proximity to low-speed streaky motions. As in the high-Reynolds-number case, conditional averaging is used to extract the local structure. Here the same conditional event is specified: a local u-minimum with $u < 0.75U_\infty$. These near-wall conditional eddies are presented in figure 12 at $y^+ = 21$ and 46, with the $y^+ = 92$ result included for completeness. The

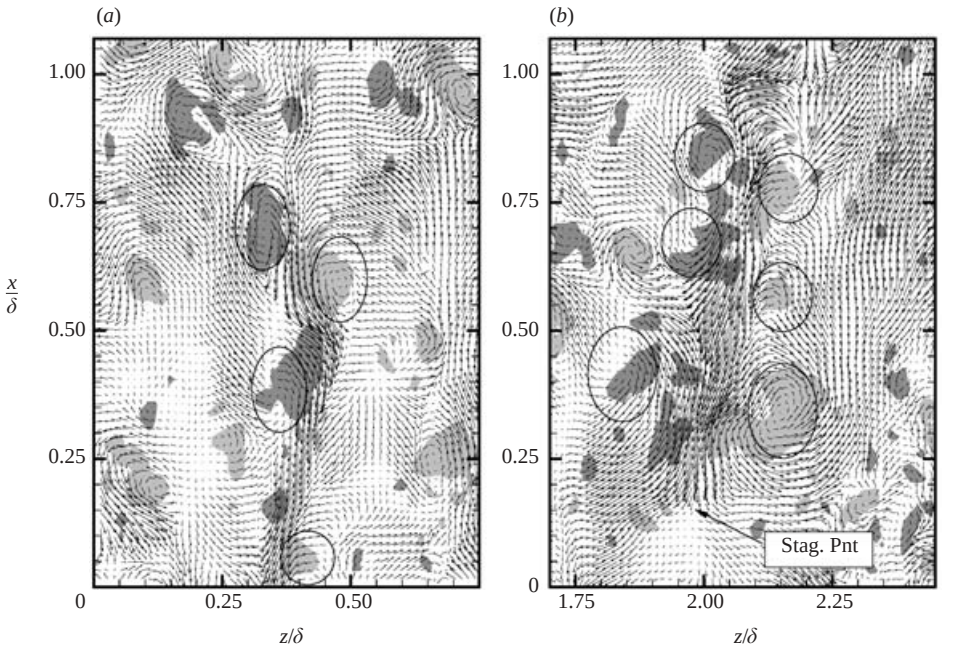

FIGURE 13. Vortex packets at $y^+ = 46$ and $Re_\theta = 1015$. Velocity vectors are plotted with $U_c = 0.65U_\infty$; grey patches are $\lambda_{ci}\omega_y/|\omega_y|$. (*a*) One-legged hairpins; (*b*) two-legged hairpins.

educed structure at $y^+ = 46$ contains all the important elements of the $(x$–$z)$-plane hairpin-vortex signature. In particular, it is noted that the streamlines of the vortices are elliptical, as expected, and clearly show a rotating pattern. Such a pattern is not explained by the existence of purely quasi-streamwise vortices, even with a slight angle to the wall. It can only be explained by the frequent occurrence of vortices with a steep angle from the wall, such as the upper legs of a hairpin-type vortex.

At $y^+ = 92$, the conditional eddy is also consistent with this interpretation. Note the increasing vortex width and vortex core size with distance from the wall, as seen in the higher Reynolds number results. The $y^+ = 21$ conditional eddy contains a similar pattern, but now the major axes of the elliptical rotation patterns are growing large relative to the minor axes. This indicates vortices with only a slight angle from the horizontal, such as the well-documented quasi-streamwise vortices (also interpreted as hairpin legs).

Furthermore, vortex organization is observed in the region $y^+ < 60$. Figure 13 contains two examples of vortex packets at $y^+ = 46$ from the same realization. The streamwise view of the measurements does not permit visualization of the larger packets in their entirety, but the organization of the structures is apparent from the data. Figure 13(*a*) reveals several asymmetric, apparently one-legged, vortex signatures aligned to extend at least 0.8δ streamwise. Regions of swirling velocity vectors are marked, and contours of swirling strength confirm the presence of vortices in these regions and elsewhere. The low-speed streak associated with these structures is also clear. Figure 13(*b*) contains three two-legged hairpin signatures, aligned at a slight angle from the streamwise coordinate. The associated low-speed region again extends approximately 0.8δ in x, and, as expected, a stagnation point is present upstream of the final vortex signature.

The conditional results in figure 12 provide evidence for the frequent occurrence of hairpin-type vortices near the wall. More importantly, the instantaneous realizations reveal the streamwise alignment of these structures at this height, providing evidence for the existence of vortex packets in the region $y^+ < 60$. These observations complement the visualization results reported in Smith (1984), in which groups of 2–5 vortices were occasionally observed to form around low-speed streaks in the approximate region $y^+ < 35$.

6. Characteristics of vortex packets

6.1. *Vortex organization*

The instantaneous realizations presented in the previous two sections reveal (i) the association of vortices with the low-momentum regions, and (ii) the organization of these vortices into long streamwise packets. The presented conditional averages provide statistical support for the first observation. In this section, we provide statistical evidence for the organization of vortices into packets.

The swirling strength, λ_{ci}, has been established as an effective tool for identifying vortices in turbulent fields. Spatial correlations of swirling strength in the (x–z)-plane, then, reveal the statistically dominant relative orientations of vortices. Contours of constant $R_{\lambda\lambda}(r_x^+, y^+, r_z^+)$ are presented in figure 14 as a function of distance from the wall at the high Reynolds number. At each height, the primary non-self-correlation peaks appear with streamwise separation, revealing that *the most probable orientation of vortices in the boundary layer is streamwise-aligned*. The correlations, of course, average over all the data, so the persistence of a peak through the correlation reveals the frequency with which this organization occurs.

Trends in the correlations reveal characteristics of the vortex packets. The separation of the vortices (i.e. the separation of the secondary and self-correlation peaks) is consistent with instantaneous realizations in the present data, and the (x–y)-plane results; $\Delta x^+ \approx 200$–250, and this separation tends to increase with distance from the wall. The width of the secondary peaks is evidence of a wide distribution of orientations; this is also evident in the instantaneous realizations. Finally, the width of the self-correlation peak increases with distance from the wall, consistent with an increase in vortex core size with y.

At $y^+ = 100$ and 220, additional non-self-correlation peaks appear, now with spanwise separation. These peaks are interpreted to be the contribution from the opposite leg in a counter-rotating vortex pair. The spanwise separation of the peaks, $\Delta z^+ \approx 100$–120, represents the average hairpin width at these heights, and is consistent with observation. The disappearance of these peaks at greater y locations is statistical evidence of the greater complexity and disorder of the flow further from the wall. Peaks at angles near 45° from the x- and z-axes would be the expected contribution from staggered arrays of one-sided vortices with opposite rotation. There is weak evidence for such a contribution in figure 14(c) and perhaps figure 14(d), but the overwhelming pattern of correlation is one consistent with streamwise alignment.

6.2. *Vortex growth*

One of the implications of Townsend's attached-eddy hypothesis is that eddy size increases in proportion to distance from the wall. In earlier sections, two spanwise lengthscales are shown to increase linearly with y: the mean width of the low-speed regions, as estimated by quantitative flow visualization, and the width of the stochastically estimated low-momentum region. The width of the conditionally

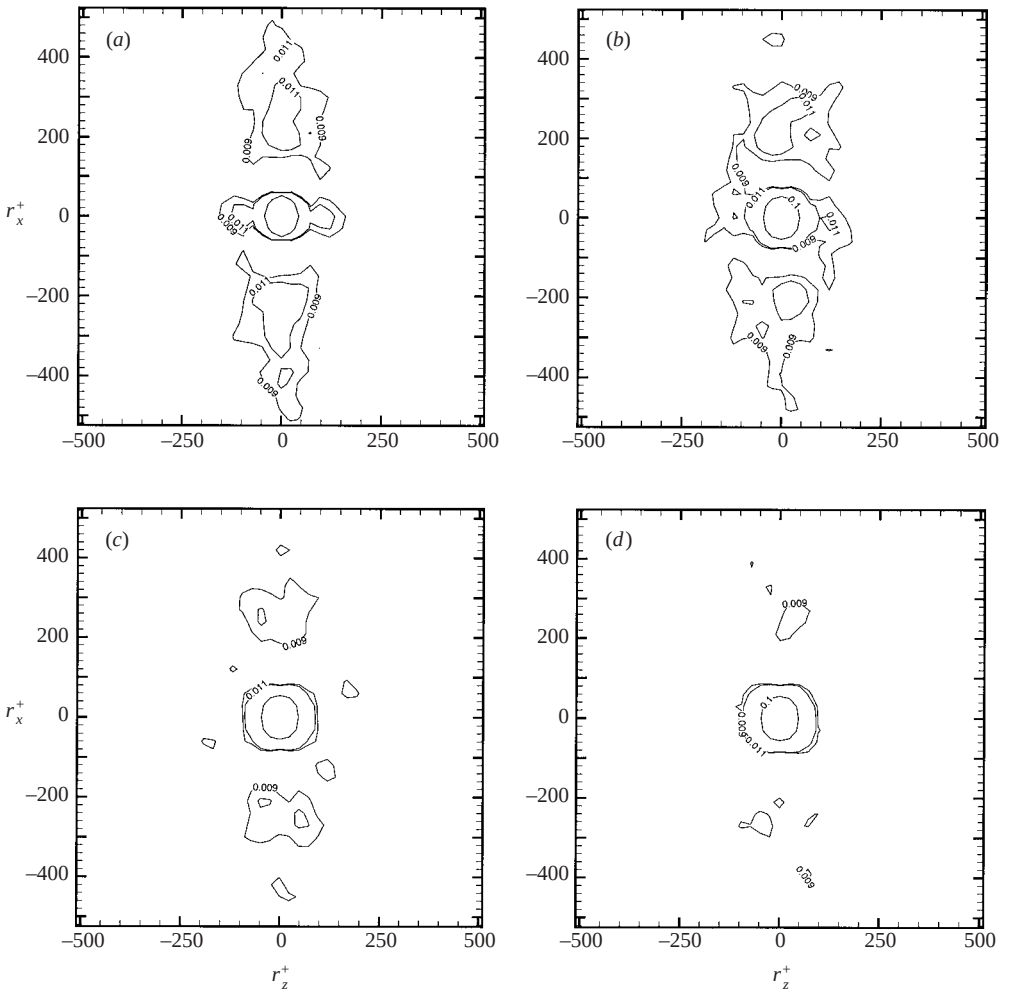

FIGURE 14. Spatial correlations of swirling strength, $R_{\lambda_{ci}\lambda_{ci}}(r_x^+, y^+, r_z^+)$, at $Re_\theta = 7705$. (*a*) $y^+ = 100$; (*b*) $y^+ = 220$; (*c*) $y^+ = 330$; (*d*) $y^+ = 440$.

extracted hairpin (shown in figure 11) may also be estimated as a measure of spanwise eddy dimension; it is plotted in figure 15. The scale is estimated by setting a threshold for the streamwise velocity to define a low-speed region associated with the structure and measuring the spanwise width of that region at $r_x^+ = 0$ (this scale is also shown above each plot in figure 11.) Figure 15 reveals that the spanwise scale of the conditional eddy varies remarkably linearly with distance from the wall, in support of the attached-eddy theory.

The linear variation of these scales with y is consistent with the idea of 'self-similar' growth of structures in an average sense, as these lengthscales are obtained by averaging over all scales in the flow at a given height. This variation does not necessarily imply, however, that each structure grows in a strictly self-similar fashion in time.

One crude but effective test of this more restrictive definition of self-similarity is based on observation of structure. In (x–y)-plane results, AMT report the observation of vortex packets in which the envelope of the vortex heads increases linearly with

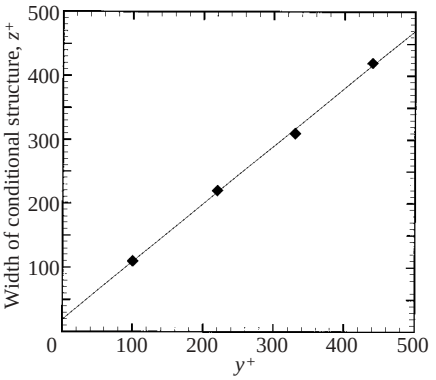

FIGURE 15. Spanwise size of conditional eddy in the $(x–z)$-plane as a function of wall-normal location.

y, forming a distinctive ramp-like shape that angles upwards from the wall. In the $Re_\theta = 7705$ layer, these ramps occur frequently, with one or more appearing in 80% of realizations at varying stages of growth. The present data, of course, are taken independently in time from the vertical-plane data, but these structures will occur with similar frequency in both experiments. Thus, if the vortices are each growing self-similarly, the horizontal-plane data will reveal vortex cores and low-momentum regions in a wedge-like shape, widening with distance downstream. The existence of wedge-shaped structures in the $(x–z)$-plane data is then a necessary but not sufficient condition for individual self-similar growth. Careful and repeated observations of the data, however, do not reveal such wedge shapes, either in regions of low momentum or in aligned vortex cores. The swirling strength correlations also support this observation. Therefore, it is concluded that *individual structures, while expected to exhibit some growth in all three dimensions, do not grow linearly over the entire course of their development in the boundary layer*. This conclusion, however, must be reconciled with the aforementioned observation that several spanwise lengthscales are consistent with self-similar growth of structures in an average sense. In the following section, a mechanism is proposed by which additional spanwise scale growth may occur.

7. Mechanisms of scale growth

7.1. *Merging of vortex packets*

Merging or pairing of structures has been proposed as a mechanism of scale growth by several authors. Perry & Chong (1982) propose merging of lambda-type vortices as a mechanism for the formation of a hierarchy of structures. The inner legs of the merging vortices cancel, and the resulting vortex is doubled in scale with similar shape. Wark & Nagib (1989) propose a model that employs the more general Perry & Chong vortex pairing mechanism, but involves hairpin-type structures at a shallower angle to the wall. In this model, the transverse dimension of the vortex doubles with pairing. Recently, this growth mechanism was observed explicitly between spanwise-interacting hairpins in the computational (DNS) channel flow data of Adrian *et al.* (2001).

In the present paper, the merging of vortex packets, and hence the merging of associated low-momentum regions, is proposed as a mechanism of spanwise scale growth. The merging occurs on an eddy-by-eddy basis by a mechanism similar to that proposed by Wark & Nagib (1989) and observed in Adrian *et al.* (2001). The

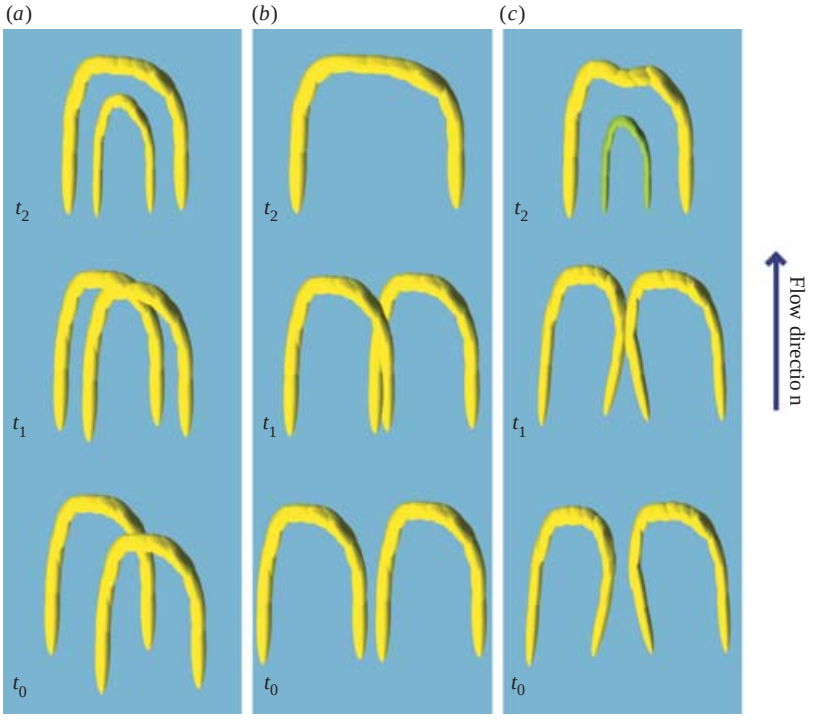

FIGURE 16. Idealized schematic of vortex merging scenarios. (*a*) Overlap and pairing of outer structure, leaving a residual vortex with rotation in the direction of the mean shear; (*b*) merging of outer structures with inner-leg annihilation; and (*c*) merging of outer structures without overlap, leaving a residual vortex with rotation opposite of the mean shear (shown in green).

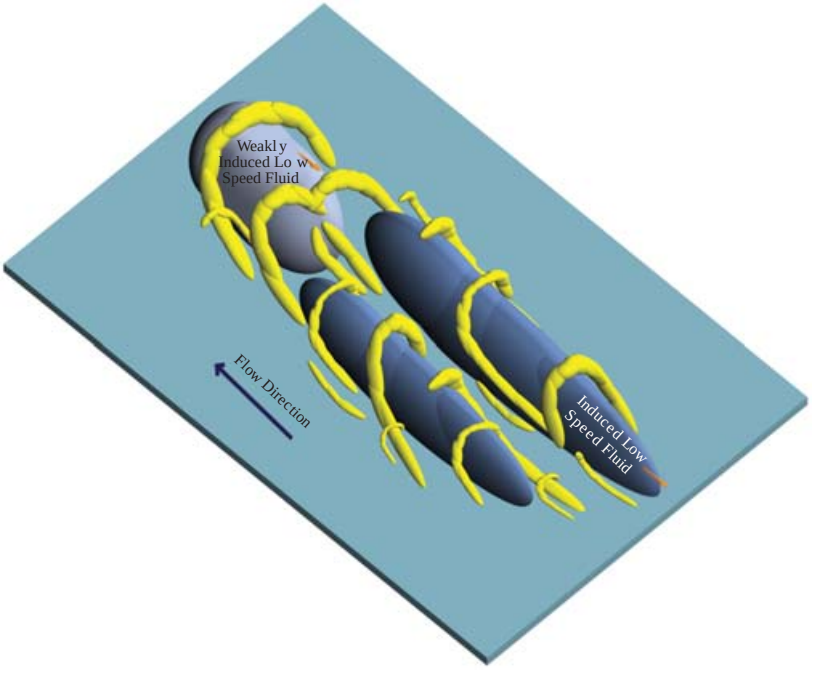

FIGURE 17. Idealized schematic of scale growth through vortex re-connection and packet merging.

extent to which adjacent packets merge simply depends on the number of vortices that merge or amalgamate. Unfortunately, the exact details of actual vortex merging processes in high-Reynolds-number turbulent boundary layers are unknown. Perry & Chong (1982), for example, assume pure leg cancellation of the Λ-type vortices, leaving only the merged portions contributing to the flow field. Wark & Nagib (1989) also assume complete annihilation of the legs of hairpin-type structures. In reality, however, an enormous range of relative vortex configurations is possible during merging, and many of these configurations may lead to merging scenarios in which the fragmented remains of the structures persist. In figure 16, three potential spanwise merging scenarios are schematically presented in highly idealized form. The structures in figure 16 are viewed from above, looking down on the wall (shown in blue) with flow direction bottom to top. Each merging scenario contains structures at three times: before (t_0), during (t_1), and after (t_2) merging.

Figure 16(a) depicts the interaction of hairpin-type vortices of comparable size, overlapped spanwise and moving with slightly different convection velocities. As the vortices intersect, viscous re-connection occurs between the larger and smaller segments of the respective structures. The result is two vortices with rotation in the direction of the mean shear ('prograde' rotation), one with larger spanwise scale and one smaller. If the merging vortices happened to be aligned spanwise, then such a streamwise interaction would result in one stronger vortex of comparable scale without a clear residual structure.

Figure 16(b) depicts an inner leg-annihilation mechanism similar to that proposed in Wark & Nagib (1989). The initial structures interact spanwise, either growing or convecting into one another, resulting in a vortex similar in shape to the vortices from which it was formed but larger in spanwise scale. The residual structures (inner legs) are assumed to mutually annihilate.

A third potential merging scenario is depicted in figure 16(c). Here, initial vortices interact spanwise, but the inner legs cross without annihilating. As in the previous two cases, the dominant resulting structure is a hairpin-type vortex of larger spanwise scale. The remaining fragments of the merged structures are also assumed to re-connect; however, this merging now creates a reverse or 'retrograde' hairpin, i.e. one rotating against the mean shear (depicted in green in figure 16(c)). Unlike a conventional hairpin, which propagates backwards and upwards against the mean shear to remain upright, this retrograde vortex would tend to propagate forward and downward while inducing fluid in the same direction. Thus, it would be expected to move quickly forward and towards the wall, while inducing a Q4 or sweep event between its legs. Evidence for the occurrence of this type of interaction is provided by the existence of retrograde vortices in (x–y)-plane data (Tomkins 1997), and the existence of forward-inducing counter-rotating vortex pairs in the present (x–z)-plane results.

It should be emphasized that these schematically depicted structures are highly idealized, and that in an actual turbulent flow their shape and aspect ratio will vary, in addition to being Reynolds-number dependent. Furthermore, other merging scenarios, not depicted here, are expected to lead to different merged structures. Hence, the structures created by merging processes in an actual flow will necessarily show a degree of variation.

A highly idealized version of the packet merging process is presented schematically in figure 17. The vortices are depicted in yellow and rotate with the mean shear. Two packets are shown, each with 4–5 vortices, and the wall is presented in light blue. The upstream, at that time separate, vortices in each packet work to induce a

local region of momentum deficit between their legs and underneath their heads; the cumulative effect of this induction is an elongated low-speed region, depicted here in dark blue. The downstream vortices in each packet have merged, or are in the process of merging, to create new structures with roughly double the spanwise scale. These larger vortices also induce low-speed flow. Due to their larger size, however, this induction is now weaker, according to Biot–Savart, and hence represented by lighter blue. (Note that this depiction is consistent with the observations presented in AMT; see e.g. figure 20.) The region between the two upstream packets now 'feels' the cumulative forward induction from the series of neighbouring vortex legs, so that a region of high-speed flow forms between them.

The altered vortex induction is expected to have an effect on the evolution of the structures after combining. With reduced backwards propagation, the larger structures will be expected to convect downstream faster. Hence, larger vortices after merging may separate from the packets from which they were created.

In reality, of course, the flow pattern will typically be extremely complex. Merging packets will often have a different number of vortices and be out of phase with respect to position. The structures may also be in different stages of growth (i.e. different sizes). Furthermore, individual vortices will often be highly asymmetric, which may create conditions more or less favourable for coalescence. Elements of this complexity are included in the schematic; however, the full range of possible configurations cannot be represented in any one depiction. Nonetheless, we may define a *vortex packet merging signature* based on the above idealization.

7.2. *Merging signature*

The vortex packet merging signature is the velocity vector pattern expected in the data if the horizontal measurement plane were to intersect two packets in the process of merging. This merging signature is presented in figure 18, and is a combination of (x–z)-plane hairpin-vortex signatures with some additional features. The upstream, unmerged, packets appear (on the bottom half of the figure) as two adjacent series of individual vortex signatures. Each induces a low-speed streak as seen in the examples given previously. The close proximity of the packets creates a region of high-speed fluid between the groups of structures, as discussed above, creating a low–high–low spanwise pattern of streamwise velocity upstream. The legs of the (downstream) merged vortices, visible in the upper half of the figure, are farther apart spanwise, and thus induce a weaker backwards flow. This backwards induction is important in the merging signature because the fluid on which it acts meets the faster moving, upstream, forward-induced fluid between the separate packets. The interface between these chunks of fluid forms a distinctive stagnation point, marked 'SP' in the figure.

As with the schematic of packet merging, the merging signature is highly idealized. It assumes symmetric vortices, equal vortex size, and that the packets are 'in phase'. Actual vortex packets in the process of merging will only approximately satisfy these assumptions, and the associated merging signature will differ from the idealization accordingly. It is hoped, however, that the idealized signature will provide a useful reference case.

The structure in figure 17 and its associated signature, although idealized, are highly complex. One disadvantage of matching to an ideal yet complex signature is that a near-exact pattern is less likely to appear in a highly turbulent flow than with a simpler pattern, because so many individual elements must appear in an idealized form. However, one advantage of such complexity is that the pattern is

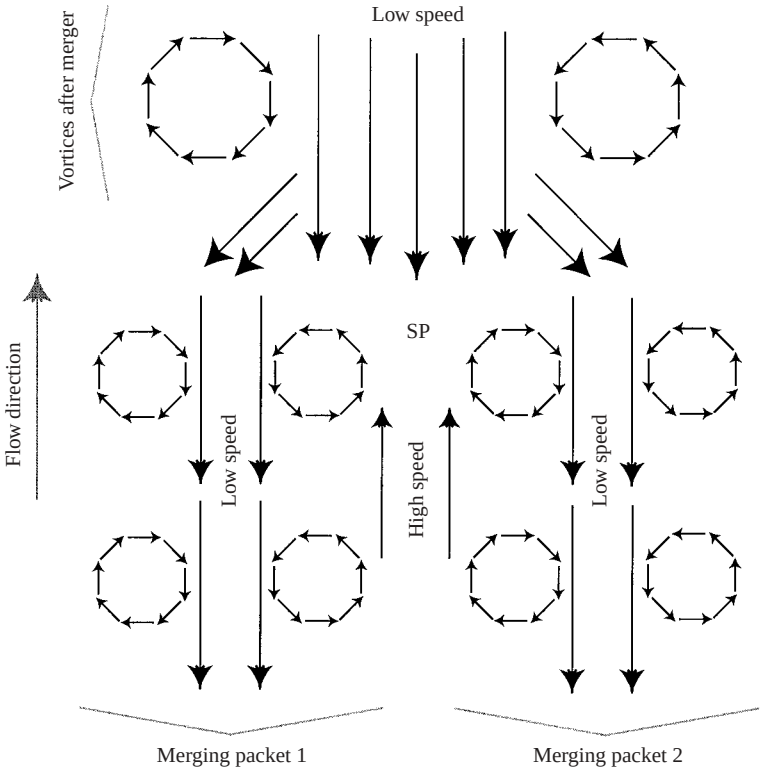

FIGURE 18. Idealized velocity vector signature of merging vortex packets, as viewed in the reference frame of the merging vortices.

quite distinctive, and thus the signature of interest will probably only be created by the proposed mechanism. In this sense, the appearance of the vortex packet merging signature is considered a moderately rigorous test for the existence of the mechanism in question.

7.3. *Evidence for mergings*

All data sets at the low Reynolds number were inspected for evidence of merging vortex packets. Interestingly, several excellent examples of the merging signature outlined above appear in the data at each wall-normal location. Three examples, one at each height, are shown in figure 19, with the flow from bottom to top. In each case, almost all of the key elements of the signature are clearly visible, including the stagnation point, which may be used to reference the other signature elements. The two swirling vector patterns (i.e. one vortex signature) expected downstream of the merge point are marked with circles and confirmed by patches of swirling strength. The two vortex signatures expected immediately upstream of the merge point (one from each merging packet) are also visible in each example, with λ_{ci} present at each of the three or four associated vortices. Examples in figures 19(*b*) and 19(*c*) also include an additional vortex signature further upstream; these are also members of the merging packets. The low-speed regions associated with both the upstream packets and the downstream merged structures are present in all examples. The high-speed region expected between the upstream packets is obvious near the merging point

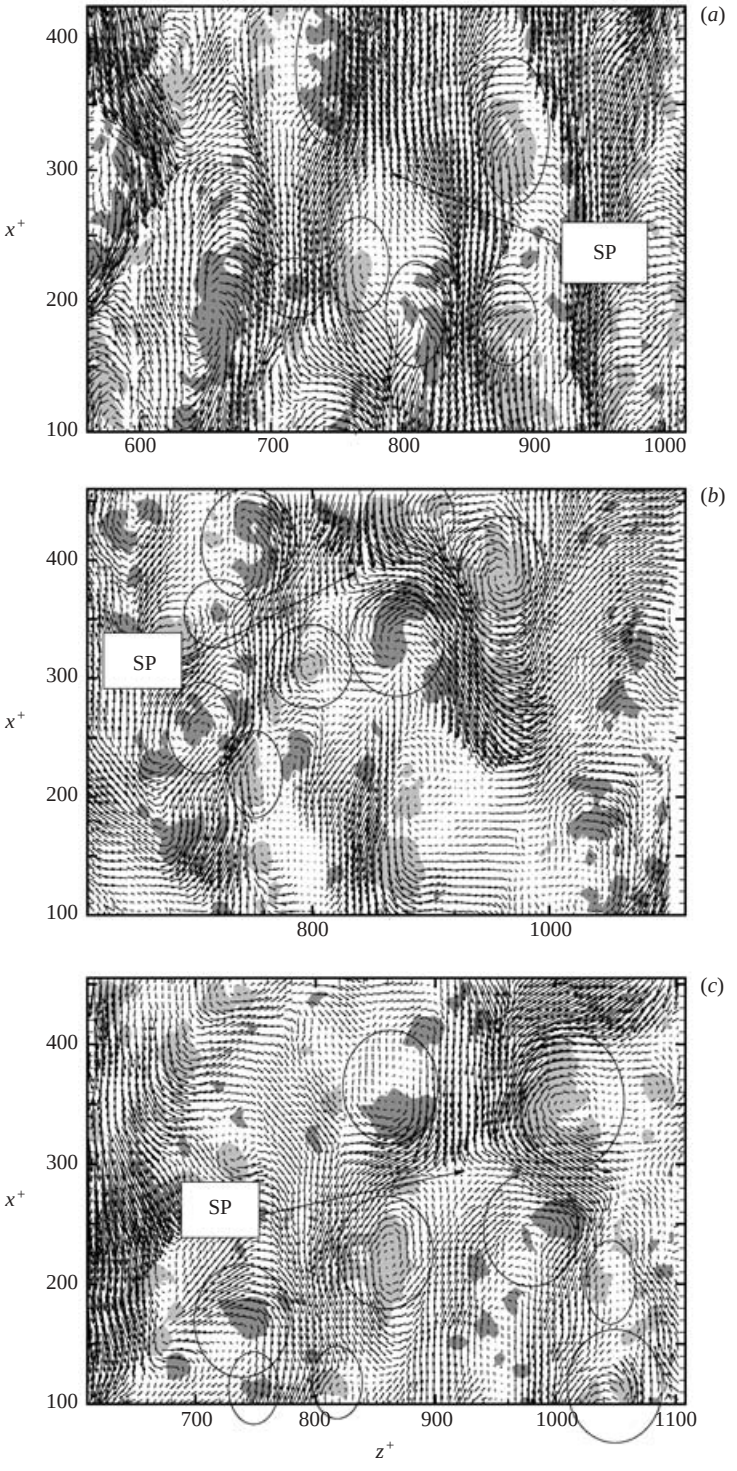

FIGURE 19. Evidence of scale growth through packet merging at $Re_\theta = 1015$. Velocity vectors and patches of $\lambda_{ci}\omega_y/|\omega_y|$. (*a*) $y^+ = 21$, $U_c = 0.65U_\infty$; (*b*) $y^+ = 46$, $U_c = 0.69U_\infty$; (*c*) $y^+ = 92$, $U_c = 0.79U_\infty$.

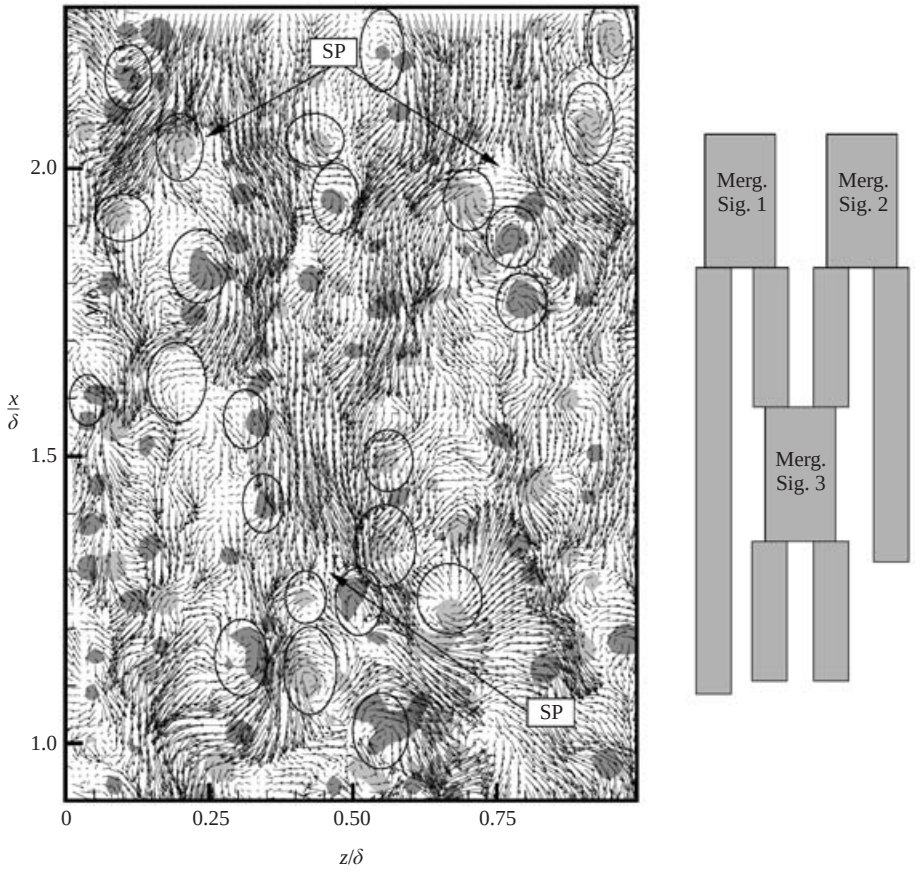

FIGURE 20. Evidence of scale growth through packet merging at $Re_\theta = 7705$ and $y^+ = 100$. Velocity vectors and patches of $\lambda_{ci}\omega_y/|\omega_y|$. $U_c = 0.65U_\infty$.

in figure19(b); in figure 19(c), this region is visible all the way from the stagnation point to the lower edge of the frame. In each case, the predicted stagnation point is distinctive.

Inspection of the high-Reynolds-number data at $y^+ = 100$ also reveals merging signatures, and although the greater complexity of the flow makes clear signatures less frequent, an example is presented in figure 20. This realization is offered in part as evidence of packet merging at $Re_\theta = 7705$, but more as an example of an unusual and interesting configuration of signatures. Three packet merging patterns appear in close proximity, all of which appear to be interacting, as depicted in the schematic adjacent to the data. Each of the signatures contains many of the defined elements, but the upstream signature, labeled 3 in the schematic, appears to merge with the upstream (not merged) portions of the two downstream signatures (1 and 2). Furthermore, the outlying unmerged portion of signature 1 appears to extend well upstream, and eventually merge with one of the unmerged packets in signature 3 (this occurs at approximately $z/\delta = 0.25$, $x/\delta = 1.0$). The outlying (not merged) packet of signature 2 also appears to extend quite far upstream, bordering signature 3. This plot is an example of the complex interactions that are expected in the boundary layer, particularly at elevated Reynolds number. In this realization, the interacting elements

are captured in a state of relative order, but it should be stated that this particular configuration is an anomaly. One possible explanation for the appearance of such a signature may be the following. Assume the existence of four vortex packets, each extending roughly the view of the figure in x and spaced closely in z. The packets may be labeled 1–4 in order from left to right. Then the signature might occur through a simple series of packet mergings: 1–2 and 3–4 at the downstream end, to create signatures 1 and 2, and the merging 2–3 at the streamwise midpoint of the figure to create signature 3.

Unfortunately, time evolution information is not available here to provide unequivocal evidence for or against the growth mechanism in question. Due to the highly distinctive nature of the packet merging signature, however, the appearance of velocity vector patterns with a remarkable resemblance to this signature at each height studied is interpreted to be convincing evidence that merging of vortex packets is an active mechanism of spanwise growth in the region $y^+ < 100$.

7.4. *Frequency of mergings*

We now wish to estimate the frequency with which these mergings occur. One approach involves visual inspection of velocity vector plots for the packet merging signature. This approach yields a relatively high number of merging identifications, which varies with y as expected. At $y^+ = 21, 46$ and 92, some 30%–35%, 40%–45%, and 25%–30% of realizations contain a merging signature, respectively. Each realization, of course, only captures a fraction of the full streamwise extent of many streaky structures, and although each captures several structures spanwise, the above percentages are nonetheless considered quite high. That is, *scale growth by merging of vortex packets appears to occur quite frequently in the approximate range* $20 < y^+ < 100$. The slight reduction in packet merging signatures observed at $y^+ = 21$ is expected based on the previous observations of quasi-streamwise vortex cores located in the range $y^+ = 20$–40 (and hence, fewer hairpin vortex signatures of any variety at $y^+ = 21$). Note that this per-realization reduction in signatures occurs despite a greater density of streaks, and a high density of streak mergings (but without the vertical vorticity present in the vortex packet merging signature). The reduced percentage at $y^+ = 92$ is probably a consequence of the greater spacing of structures at that height.

One drawback of this approach is the degree of subjectivity involved. Patterns with almost all of the defined elements of the signature, like those in figure 19, are readily identified. Many patterns, however, have some but not all of the signature elements, and identification of the pattern as a signature becomes subjective. Thus, a more objective approach is sought to corroborate the above observations.

One such approach is to search for the signature or footprint that merging packets leave in the velocity field. The low-speed regions induced by groups of vortices are often more readily visualized than the vortices themselves. The low-speed region in a merging signature is simply a fork, with the thick (merged) end of the fork downstream, the thinner (not merged) ends of the fork upstream, and a high-speed region between the fork legs. Inspection of contours of streamwise velocity for this simple pattern is considered an objective evaluation of the frequency of merging low-speed regions.

Small-scale fluctuations in the velocity field were found to occasionally create small patterns in the contours, by random chance, that are similar to the one described above. The current interest, of course, is in the merging frequency of larger scales,

i.e. groups of vortices. Thus, a filter is applied to the data in order to remove the small fluctuations and leave only the scales of interest. As in the earlier procedure, the filter is applied in wavenumber space as a sharp cutoff, although now the filtering is performed in the streamwise direction (spanwise filtering was found to often smear out the smaller, merging structures). The cutoff wavenumber corresponds to a wavelength of $\lambda_{x,c}^{+} = 200$, and the u-contour level defining a low-speed region is set at 95% of the local mean velocity.

The following procedure is used in counting. In each realization, the total number of low-speed streaks was determined. Then, the merging patterns in the data were identified, and the number of streaks involved in such a pattern was recorded. Thus, the procedure determines the percentage of streaks involved in a merging pattern over a streamwise view of 460 viscous wall units (1.08δ). Near the wall ($y^{+} = 21$), 45% of streaks are in a merging pattern. At $y^{+} = 46$, the figure drops to 33%, and at $y^{+} = 92$, the figure is 27%. Thus, the coalescence of low-speed regions occurs very frequently in the region $y^{+} < 30$, as observed by Nakagawa & Nezu (1981) and Smith & Metzler (1983). As expected, the frequency is slightly reduced further from the wall as the spacing of the streaks increases. However, the percentage remains significant at these heights, providing further evidence that merging is an important mechanism for scale growth up to $y^{+} \approx 100$ in a low-Reynolds-number layer.

Inspection of the velocity contour plots also reveals forks oriented in the opposite direction, i.e. with the merged end downstream, and the forked or split end upstream. The frequency with which this 'upstream fork' pattern occurs in the data is not insignificant: at $y^{+} = 21$, 46, and 92, the percentage of streaks in such a pattern is 19, 17 and 5, respectively. Some streaks, of course, are in both an upstream and downstream fork. Interpretation of this (upstream fork) pattern is difficult without time-evolution information. It may, like the downstream fork, represent a coalescence, but with initial merging occurring between upstream elements. Alternatively, the upstream fork may represent a divergence of one structure or set of structures into two. This interpretation is consistent with the results of Smith & Metzler (1983), who observed both merging (with greater frequency) and splitting (with lesser frequency) of streaks in the near-wall region.

A similar procedure is performed on the $Re_{\theta} = 7705$ data at $y^{+} = 100$. Inspection of the data reveals that 30% of low-speed regions are involved in a merging pattern, very close to the figure of 27% observed at $y^{+} = 92$ in the low-Re results, and that 9% of streaks are involved in an upstream fork pattern.

In summary, an estimation technique based on counting of u-velocity contour patterns demonstrates that merging of low-speed structures is a means of scale growth up to $y^{+} = 100$ at both low and high Reynolds numbers. Furthermore, a procedure based on inspection of velocity vector maps for a defined signature reveals that merging of vortex packets is an active mechanism by which this coalescence occurs.

8. Summary and conclusions

The structure of turbulent boundary layers has been investigated using PIV in the horizontal plane. Wide-view digital measurements are obtained at several heights throughout the upper buffer layer and logarithmic region at $Re_{\theta} = 1015$ and 7705. Additional measurements are performed at selected heights with large-format film to capture the large scales in both x and z with high resolution. The investigation builds upon the (x–y)-plane study of AMT, in which hairpin-type vortices were observed

to organize in the streamwise direction to create motions of much larger scale. The goal of the present study is to develop a three-dimensional picture of boundary-layer structure.

Inspection of instantaneous realizations reveals that the dominant large-scale motions at elevated Reynolds number are regions of low u-momentum elongated in the streamwise direction. These motions are shown to extend 2δ or more streamwise, and typically 0.1δ–0.4δ spanwise, and grow with distance from the wall. Linear stochastic estimation is used to approximate the conditional average based on a simple low-u event; this result provides statistical support for the existence and importance of large, elongated, low-speed motions in the outer layer.

Significant supporting evidence for the vortex packet model of AMT is found throughout the logarithmic region (i.e. from $y^+ = 100$ to $y/\delta = 0.2$) at $Re_\theta = 7705$. At each height investigated, the observed low-momentum regions (LMRs) are consistently associated with swirling or vortical motions, aligned in x, that act to induce flow backwards. Close inspection of many younger, smaller LMRs reveals that these structures are simply concatenations of one- or two-legged hairpin vortex signatures that propagate downstream together with roughly equal convection velocity. Examination of larger, older structures farther from the wall requires a vortex identification technique (λ_{ci}) in conjunction with vector patterns to effectively extract the organized motions. In more complex examples, e.g. data closer to the wall in which several structures of disparate scale are superimposed, filtering is necessary to separate the scales of interest from the fluctuations. However, in the above examples and throughout the data, it is shown that proper analysis reveals organized vortical structure in clear support of the vortex packet paradigm.

Data at the low Reynolds number provide new evidence for the presence and organization of hairpin-type vortices in the region $y^+ < 60$. Velocity vector patterns (HVS) are observed that cannot be explained by the existence of quasi-streamwise vortices alone, and the signatures organize streamwise. These buffer-layer results are important for two reasons. First, they provide clear quantitative evidence for the existence of hairpins near the wall, complementing the visual studies of Smith and co-workers, in a region for which consensus on the dominant structure is lacking. Furthermore, the observations of structural organization provide evidence for the occurrence of vortex packets down to $y^+ = 46$.

The present results also provide statistical evidence for two important aspects of the vortex packet paradigm. First, spatial correlations of swirling strength throughout the logarithmic region at high Reynolds number reveal that the most probable orientation of successive vortices is streamwise-aligned. This result complements the $(x–y)$-plane channel flow measurements of Christensen & Adrian (2001), which show a statistical footprint of inclined vortex packets. Secondly, by specifying a simple local minimum in velocity below some threshold, we educe the hairpin vortex signature from the data at all heights and at both Reynolds numbers investigated. These conditional results establish the hairpin vortex as the dominant small-scale structure, and statistically link the hairpin with the low-momentum regions. The near-wall conditional eddies may also be pointed to as further evidence for the existence of hairpins at $y^+ = 46$, and even at $y^+ = 21$.

The final and perhaps most important contribution is in the understanding of scale growth in the boundary layer. Mean values of three spanwise lengthscales (based on quantitative visualization, stochastic estimation, and conditional averaging) are shown to vary linearly with distance from the wall. This linear increase is consistent with individual self-similar growth in time, but is not proof of it. In fact, inspection of the

present data, in conjunction with previous (x–y)-plane results, suggests that individual structures do not grow strictly self-similarly over the course of their development.

Instead, the merging of vortex packets on an eddy-by-eddy basis is proposed as a mechanism by which additional spanwise scale growth, and hence the observed linear scale variation, may occur. This model draws upon the vortex leg re-connection mechanism proposed in Wark & Nagib (1989). The extent to which packets merge simply depends on the number and relative location of individual vortices that pair or coalesce. At the point of meeting, the merging structures are expected to leave a highly distinctive footprint or signature in the flow field. The appearance of this distinctive signature with high frequency in the data (e.g. 40%–45% of realizations contain such a pattern at $y^+ = 46$) is considered substantial evidence that merging of vortex packets is an important mechanism of spanwise growth in boundary layers up to $y^+ = 100$.

The present model provides a link between previous observations and conjectures. The visual studies of Smith & Metzler (1983) and Nakagawa & Nezu (1981) provide observations of frequent streak merging for $y^+ < 30$. Farther from the wall, the increasing complexity of the flow makes objective evaluation of coalescence difficult, so direct observations are not reported, although streak merging is conjectured by both researchers as a means of growth. The vortex re-connection mechanism of Perry & Chong (1982) is also an interesting proposition, and has been employed in previous models of boundary-layer growth (e.g. Wark & Nagib 1989). This vortex merging model, however, while able to explain the development of a hierarchy of structures, does not offer an explanation for the one growth mechanism supported by direct observation: the merging of elongated low-speed regions. The present model, though, provides a logical bridge between the two concepts, employing the vortex-pairing mechanism within the framework of the vortex packet paradigm to explain the observed coalescence of long regions of momentum deficit.

This model has implications for fundamental concepts in boundary layers. As Adrian *et al.* (2001) discuss, the logarithmic law and von Kármán's constant are most probably embodiments of fundamental aspects of the eddy structure in wall turbulence. Hence, prediction of basic behaviour, such as the value of von Kármán's constant, requires a thorough understanding of this structure and how it varies with distance from the wall. The concept of self-similar growth is fundamental to the logarithmic law. The vortex packet model, presented in AMT and extended here, allows for streamwise scale growth through the creation of new vortices, and streamwise and wall-normal growth by stretching due to shear. The merging mechanism proposed here permits commensurate scale growth in the spanwise direction, and hence, self-similar growth in a statistical sense.

This research was supported by the Office of Naval Research under Grants N00014-99-1-188 and N00014-97-1-0109.

REFERENCES

Adrian, R. J. 1975 On the role of conditional averages in turbulence theory. In *Turbulence in Liquids*, pp. 323–332. University of Missouri, Rolla, Missouri.

Adrian, R. J. 1988 Statistical properties of particle image velocimetry measurements in turbulent flow. In *Laser Anemometry in Fluid Mechanics-III* (ed. R. J. Adrian, T. Asanuma, D. F. G. Durao, F. Durst & J. H. Whitelaw), pp. 115–129. Springer.

Adrian, R. J. 1991 Particle-imaging techniques for experimental fluid mechanics. *Annu. Rev. Fluid Mech.* **23**, 261–304.

ADRIAN, R. J. 1997 Dynamic ranges of velocity and spatial resolution of particle-image velocimetry. *Meas. Sci. Tech.* **8**, 1393–1398.

ADRIAN, R. J., BALACHANDER, S. & LIU, Z.-C. 2001 Spanwise growth of vortex structure in wall turbulence. *KSME Intl J.* **15**, 1741–1749.

ADRIAN, R. J., CHRISTENSEN, K. T. & LIU, Z.-C. 2000*a* Analysis and interpretation of instantaneous turbulent velocity fields. *Exps. Fluids* **29**, 275–290.

ADRIAN, R. J., MEINHART, C. D. & TOMKINS, C. D. 2000*b* Vortex organization in the outer region of the turbulent boundary layer. *J. Fluid Mech.* **422**, 1–54 (referred to herein as AMT).

BLACKWELDER, R. F. & ECKELMANN, H. 1979 Streamwise vortices associated with the bursting phenonmenon. *J. Fluid Mech.* **94**, 577–594.

BROWN, G. L. & THOMAS, A. S. W. 1977 Large structure in a turbulent boundary layer. *Phys. Fluids* **20**, 243–252.

CHRISTENSEN, K. T. 2000 Time-derivative measurements in turbulent channel flow. PhD thesis, Department of Theoretical and Applied Mechanics, University of Illinois at Urbana-Champaign.

CHRISTENSEN, K. T. & ADRIAN, R. J. 2001 Statistical evidence of hairpin vortex packets in wall turbulence. *J. Fluid Mech.* **431**, 433–443.

CHRISTENSEN, K. T., SOLOFF, S. M. & ADRIAN, R. J. 2000 Piv sleuth: integrated particle image velocimetry (PIV) interrogation/validation software. *TAM Rep.* 943. Department of Theoretical and Applied Mechanics, University of Illinois at Urbana-Champaign.

GRIFFIN, O. M., RAMBURG, S. E., VOTAW, C. W. & KELLEHER, M. D. 1973 The generation of liquid aerosols for the visualization of oscillatory flows. *Tech. Rep.* Naval Research Laboratory.

GUEZENNEC, Y. G. 1985 Documentation of large coherent structures associated with wall-layer events in turbulent boundary layers. PhD thesis, Department of Mechanical Engineering, Illinois Institute of Technology.

GUEZENNEC, Y. G., PIOMELLI, U. & KIM, J. 1987 Conditionally-averaged structure in wall-bounded turbulent flow. *Tech. Rep.* CTR-S87. Centre for Turbulence Research, Stanford University.

HEAD, M. R. & BANDYOPADHYAY, P. 1981 New aspects of turbulent boundary-layer structure. *J. Fluid Mech.* **107**, 297–338.

HEIST, D. K., HANRATTY, T. J. & NA, Y. 2000 Observations of the formation of streamwise vortices by rotation of arch vortices. *Phys. Fluids* **12**, 2965–2975.

KASAGI, N. 1988 Structural study of near-wall turbulence and its heat transfer mechanism. In *Near-wall Turbulence* (ed. S. J. Kline & N. H. Afgan), pp. 596–619. Hemisphere.

KASAGI, N., IIIRATA, M. & NISHINO, K. 1986 Streamwise pseudo-vortical structures and associated vorticity in the near-wall region of a wall-bounded turbulent shear flow. *Exps. Fluids* **4**, 309–318.

KIM, J., MOIN, P. & MOSER, R. 1987 Turbulent statistics in fully developed channel flow at low Reynolds number. *J. Fluid Mech.* **177**, 133–166.

KLEWICKI, J. C., METZGER, M. M., KELNER, E. & THURLOW, E. M. 1995 Viscous sublayer flow visualizations at $R_\theta \approx 1,500,000$. *Phys. Fluds* **7**, 857–863.

KLINE, S. J., REYNOLDS, W. C., SCHRAUB, F. A. & RUNSTADLER, P. W. 1967 The structure of turbulent boundary layers. *J. Fluid Mech.* **30**, 741–773.

KOVASZNAY, L. S. G., KIBENS, V. & BLACKWELDER, R. F. 1970 Large-scale motion in the intermittent region of a turbulent boundary layer. *J. Fluid Mech.* **41**, 283–325.

KROGSTAD, K. A. & ANTONIA, R. A. 1994 Structure of turbulent boundary layers on smooth and rough walls. *J. Fluid Mech.* **277**, 1–21.

LIU, Z.-C., ADRIAN, R. J. & HANRATTY, T. J. 1996 A study of streaky structures in a turbulent channel flow with particle image velocimetry. In *Proc. 8th Intl Symp. on Application of Laser Technology to Fluid Mechanics, Lisbon, Portugal* (ed. R. Adrian, D. Durão, F. Durst, M. Heitor, M. Maeda & J. Whitelaw). Springer.

MARUSIC, I. 2001 On the role of large-scale structures in wall turbulence. *Phys. Fluids* **13**, 735–743.

MARUSIC, I. & PERRY, A. E. 1995 A wall-wake model for the turbulence structure of boundary layers. Part 2. Further experimental support. *J. Fluid Mech.* **298**, 389–407.

MEINHART, C. D. 1994 Investigation of turbulent boundary layer structure using particle-image velocimetry. PhD thesis, Department of Theoretical and Applied Mechanics, University of Illinois at Urbana-Champaign.

Meinhart, C. D. & Adrian, R. J. 1995 On the existence of uniform momentum zones in a turbulent boundary layer. *Phys. Fluids* **7**, 694–696.

Naguib, A. M. & Wark, C. E. 1992 An investigation of wall-layer dynamics using a combined temporal filtering and correlation technique. *J. Fluid Mech.* **243**, 541–560.

Nakagawa, H. & Nezu, I. 1981 Structure of space-time correlations of bursting phenomena in an open-channel flow. *J. Fluid Mech.* **104**, 1–43.

Nychas, S. G., Hershey, H. C. & Brodkey, R. S. 1973 A visual study of turbulent shear flow. *J. Fluid Mech.* **61**, 513–540.

Perry, A. E. & Chong, M. S. 1982 On the mechanism of wall turbulence. *J. Fluid Mech.* **119**, 173–217.

Perry, A. E., IIenbest, S. & Chong, M. S. 1986 A theoretical and experimental study of wall turbulence. *J. Fluid Mech.* **165**, 163–199.

Perry, A. E. & Marusic, I. 1995 A wake model for the turbulence structure of boundary layers. Part 1. Extension of the attached eddy hypothesis. *J. Fluid Mech.* **298**, 361.

Prasad, A. K., Adrian, R. J., Landreth, C. C. & Offutt, P. W. 1992 Effect of resolution on the speed and accuracy of particle image velocimetry interrogation. *Exps. Fluids* **13**, 105–116.

Robinson, S. K. 1991 Coherent motions in the turbulent boundary layer. *Annu. Rev. Fluid Mech.* **23**, 601–639.

Smith, C. R. 1984 A synthesized model of the near-wall behavior in turbulent boundary layers. In *Proc. 8th Symp. of Turbulence* (ed. J. Zakin & G. Patterson), pp. 299–325. University of Missouri-Rolla.

Smith, C. R. & Metzler, S. P. 1983 The characteristics of low-speed streaks in the near-wall region of a turbulent boundary layer. *J. Fluid Mech.* **129**, 27–54.

Smith, C. R. & Schwartz, S. P. 1983 Observation of streamwise rotation in the near-wall region of a turbulent boundary layer. *Phys. Fluids* **26**, 641–652.

Smith, C. R., Walker, J. D. A., Haidari, A. H. & Sobrun, U. 1991 On the dynamics of near-wall turbulence. *Phil. Trans. R. Soc. Lond.* A **336**, 131–175.

Soloff, S. M. 1998 An investigation of the small-scale structure in a turbulent pipe flow using high resolution particle image velocimetry. Master's thesis, Department of Theoretical and Applied Mechanics, University of Illinois at Urbana-Champaign.

Theodorsen, T. 1952 Mechanism of turbulence. In *Proc. 2nd Midwestern Conf. on Fluid Mechanics*, pp. 1–19. Ohio State University.

Tomkins, C. D. 1997 A particle image velocimetry study of coherent structures in a turbulent boundary layer. Master's thesis, Department of Mechanical and Industrial Engineering, University of Illinois at Urbana-Champaign.

Tomkins, C. D. & Adrian, R. J. 2003 Energetic spanwise modes in a turbulent boundary layer. In preparation.

Townsend, A. A. 1976 *The Structure of Turbulent Shear Flow*, 2nd edn. Cambridge University Press.

Wallace, J. M. 1982 On the structure of bounded turbulent shear flow: a personal view. In *Developments in Theoretical and Applied Mechanics XI* (ed. T. J. Chung), p. 509. University of Alabama-Huntsville.

Wallace, J. M. 1985 The vortical structure of bounded turbulent shear flow. In Lecture Notes in Physics (ed. G. E. A. Meier & F. Obermeier), pp. 253–268. Springer.

Wark, C. E. & Nagib, H. M. 1989 Relation between outer structures and wall-layer events in boundary layers with and without manipulation. In *Proc. 2nd IUTAM Symp. on Structure of Turbulence and Drag Reduction*, pp. 467–474, *Zurich, Switzerland* (ed. A. Gyr). Springer.

Wark, C. E. & Nagib, H. M. 1991 Experimental investigation of coherent structures in turbulent boundary layers. *J. Fluid Mech.* **230**, 183–208.

Westerweel, J. 1997 Fundamentals of digital particle image velocimetry. *Meas. Sci. Tech.* **8**, 1379–1392.

Zhou, J., Adrian, R. J., Balachandar, S. & Kendall, T. M. 1999 Mechanisms for generating coherent packets of hairpin vortices in channel flow. *J. Fluid Mech.* **387**, 353–396.